"Hot" in Plasmonics: Temperature-Related Concepts and Applications of Metal Nanostructures

Christian Kuppe, Kristina R. Rusimova, Lukas Ohnoutek, Dimitar Slavov, and Ventsislav K. Valev*

Recent advances in nonlinear optics, hot electrons for renewable energy (e.g., solar cells and water-splitting), acousto-optics, nanometalworking, nanorobotics, steam generation, and photothermal cancer therapy are reviewed here. In all these areas, one of the key enabling properties is the ability of metallic nanoparticles to harvest and control light at the subwavelength scale by supporting coherent electronic oscillations, called localized surface plasmon resonances (LSPRs). Various physical properties and potential areas of application emerge depending on the decay mechanism of the LSPR and, especially, depending on the considered timescale. The field of plasmonics has mainly been associated with manipulating electromagnetic near-fields at the nanoscale, where absorption is an obstacle. However, plasmonic absorption leads to a stream of temperature-related phenomena that have only recently attracted significant attention. The goal of this review is to highlight exciting new areas of research (such as nanorobotics, nanometalworking, or acousto-optical techniques) and to survey the most recent progress in more established areas (such as hot electrons, photothermal therapy, and plasmonic steam generation). To set each research area in context, the text is organized around the thermal cycle of the nanoparticles.

1. Introduction

The ability of metallic nanoparticles (NPs) to manipulate and harvest light on the subwavelength scale by supporting electronic

resonances, called localized surface plasmons (LSPs), is key for a plethora of exciting applications, ranging from renewable energy (e.g., solar or water splitting) to photothermal cancer therapy, see **Figure 1**.

Light incident on a metal can excite resonant coherent oscillations of the free (conduction band) electrons called "plasmons." These oscillations result from the competing effects of the electric force in the electromagnetic wave and the restoring force of positive nuclei. Plasmons occur at the frequency of the light and, in the case of gold, the average distance travelled by an electron in one oscillation time period is ≈6 Å.[1] The word "plasmon" can refer to three specific phenomena, depending on context. Bulk plasmons are a 3D oscillation of the electron density. Propagating surface plasmon polaritons (SPPs) are similar oscillations, propagating across surfaces or along waveguides. Localized surface plasmon resonances (LSPRs) are oscillations that take place in illuminated metal nanoparticles (see Figure 1, top panel) and they are confined to the nanoparticles. In this review, we focus on LSPRs.

LSPRs can be very pronounced, resulting in materials with strong optical responses. Metals have large electron densities (for Au, the free electron concentration is ≈5.9×10^{22} cm^{-3}),[2] consequently in plasmons, there are many oscillating electrons resulting in the generation of large electric fields. At the surface of the nanoparticle, the incident electric field can be increased by a factor of ≈10^3. Moreover, these resonances are highly tunable.

The frequency of the LSPRs in metals can cover the UV, visible, and near-IR region of the spectrum. It depends on several parameters, such as the size of the nanoparticle; red-shifting with increasing diameter of spherical nanoparticles. It also depends on the nature of the metal; although in principle, Na, K, Al, Co, Ni, Pt, Pd, etc., can sustain LSPRs, practical consideration (such as strong oscillation damping, material stability in air/water, etc.) are often an obstacle.[3] The most widely used plasmonic materials are Ag and Au. The frequency of the LSPRs also depends on the shape of the nanoparticle; in a nanorod, the LSPR along the main axis of the rod red-shifts with increasing length.[4,5] Moreover, plasmonic electron density fluctuations can be dipolar, quadrupolar, or octupolar in nature and the shape of the nanoparticle plays a role in selecting that nature. Importantly, the environment of the nanoparticle also

Dr. C. Kuppe, Dr. K. R. Rusimova, L. Ohnoutek, Prof. V. K. Valev
Centre for Photonics and Photonic Materials
University of Bath
Bath BA2 7AY, UK
E-mail: v.k.valev@bath.ac.uk
Dr. C. Kuppe, Dr. K. R. Rusimova, L. Ohnoutek, Prof. V. K. Valev
Centre for Nanoscience and Nanotechnology
University of Bath
Bath BA2 7AY, UK
Dr. D. Slavov
Institute of Electronics
BAS, 72 Tzarigradsko Shosse blvd 1784, Sofia, Bulgaria

**ADVANCED
SCIENCE NEWS**

www.advancedsciencenews.com

**ADVANCED
OPTICAL
MATERIALS**

www.advopticalmat.de

influences the frequency of LSPRs; increasing the refractive index of the surrounding dielectric causes a red-shift, which is key for many sensing applications of plasmonics.[6]

The field of plasmonics was initially envisioned to have applications in manipulating electromagnetic fields at subwavelength scales. Plasmons can strongly concentrate incident light into highly localized regions at the surface of nanoparticles; bringing two nanoparticles ≈1 nm apart from each other increases the electromagnetic field in the gap by a factor of up to 10^6.[7] Such regions of intense fields are referred to as electromagnetic "hotspots" (see Figure 1, right panel). These hotspots find applications in surface spectroscopies, including surface-enhanced Raman scattering and nonlinear optical techniques.[8,9]

Nonlinear optics (NLO) offers an increasing range of practical applications, following technological advances in ultrashort pulse lasers.[10] For commercial lasers, these advances include greater wavelength range, shorter pulses, higher power, reduced cost and automatic operation. Some of the most promising areas of applications for NLO are miniaturized tunable lasers, ultrathin optical components (based on metasurfaces), nondestructive imaging and ultrasensitive material characterization. In each case, the electromagnetic hotspots of plasmonic nanoparticles can play a crucial role.[11]

For ultrashort pulse lasers, tuning the wavelength can be achieved by frequency mixing. The simplest example of frequency mixing (and the first NLO effect to be discovered) is second harmonic generation (SHG),[12] where two photons of the same frequency are combined into a single photon at twice the frequency. Dedicated NLO crystals (several mm long) are used to achieve high efficiency of the process. Miniaturizing this technology requires materials with very strong nonlinearity, which greatly benefits from including plasmonic nanomaterials. By design of the hotspot location, these nanomaterials serve to focus light into the nonlinear material, boosting the frequency conversion efficiency.

Metasurfaces consist of a monolayer of nanostructures, whose dimensions are smaller than the wavelength of illumination.[13] The discovery of the generalized Snell's law[14] in these ultrathin materials enabled control over the amplitude, polarization and direction of the outgoing beam. NLO metasurfaces provide an additional degree of control over the frequency of the outgoing beam. Because of lower loss compared to metals, dielectric metasurfaces are often more attractive. However, plasmonic nanoparticles are easier to fabricate, compared to dielectric nanostructures, leading to significant research in NLO plasmonic metasurfaces.

In biology, NLO imaging (also known as multiphoton imaging/microscopy) includes SHG, third-harmonic generation, two-photon luminescence and Raman techniques.[15] In each case, detecting a strong signal requires high-power illumination—ideally, just below the laser damage threshold of tissue or label/photoluminescent tag molecules to prevent photo bleaching. Here too, plasmonic nanoparticles offer significant advantages, especially those made of gold. Because gold is biocompatible and its surface is easily functionalized with ligands, gold nanoparticles can serve as convenient biolabels. Compared to molecular labels or biological materials, gold nanoparticles offer strong frequency conversion and they are much more resistant to photodamage. Consequently, it is possible to image

Kristina Rusimova is a Prize Fellow at the University of Bath. Her research interests include atomic manipulation, hot electron transport, optical fiber fabrication, plasmonics, and alkali metal vapor spectroscopy. She obtained her first degree at the University of Birmingham (2012) and Ph.D. in nanoscience at the University of Bath (2016). Following a short postdoctoral position in photonics, she joined the Department of Physics at the University of Bath as an independent research fellow in 2018 working at the frontier between nanoscience and photonics.

Lukas Ohnoutek obtained his master's degree in optics and optoelectronics from the Charles University in Prague, Czech Republic. Afterward, he joined the EPSRC Centre for doctoral training in condensed matter physics (CDT-CMP) based at the Universities of Bath and Bristol, UK. He is currently pursuing a Ph.D. under the supervision of Prof. Valev. His research focuses mainly on nonlinear optical properties of plasmonic nanostructures.

Ventsislav K. Valev is a professor of physics and research fellow of the Royal Society, in the Department of Physics, at the University of Bath. Prior to Bath, he was a research fellow in the Cavendish Laboratory, at the University of Cambridge. He received his Ph.D. in 2006 from Radboud University Nijmegen, the Netherlands. His research group builds laser experiments on novel materials, such as plasmonic nanostructures, metamaterials, 2D materials, and quantum optical materials. He aims to discover new properties and to test theoretical predictions, seeking out new and useful intersections between classical electromagnetism and quantum mechanics.

with reduced illumination power and the likelihood of photodamage to cells and tissue is reduced.

NLO effects are sensitive to the structure of materials, as well as to their electric and magnetic properties.[16] In comparison to their linear optical counterparts, the NLO effects offer greater sensitivity, due to higher signal-to-noise ratios. These ratios
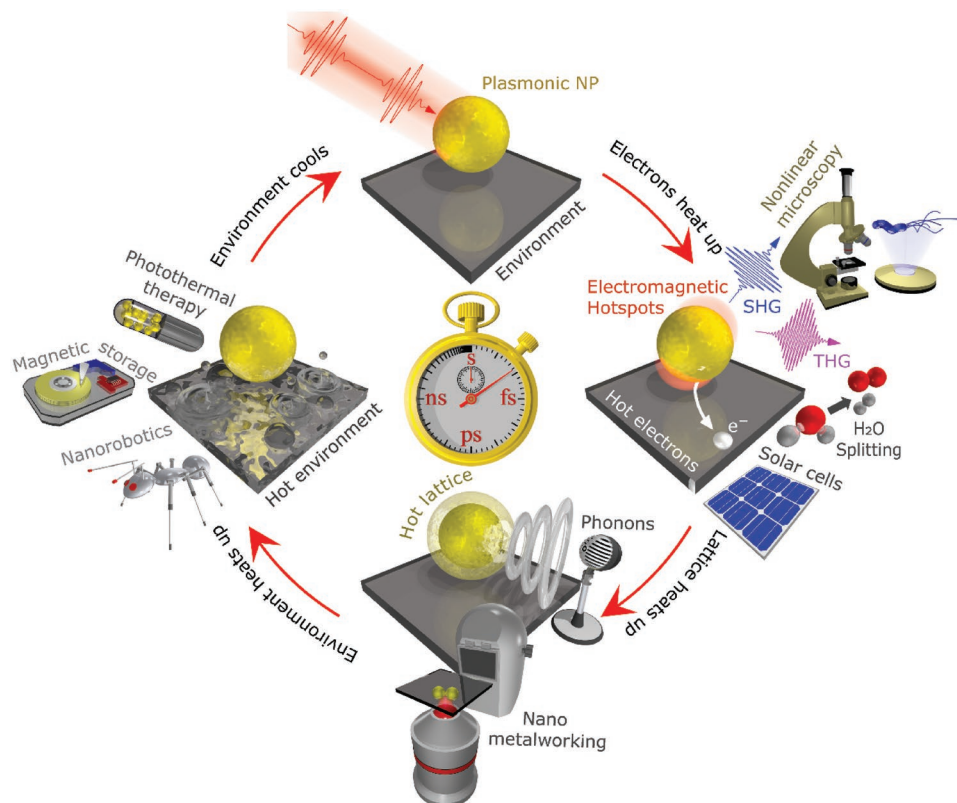
Figure 1. Temperature cycle in plasmonic nanoparticles upon illumination. Following illumination of the nanoparticles, at the femtosecond (fs) timescale, the surface plasmons produce electromagnetic hotspots. These hotspots can enhance nonlinear optical processes, such as second harmonic generation (SHG) and third harmonic generation (THG), for advanced imaging applications. Hot electrons can also be created, finding applications in solar cells and water splitting. Subsequently, at the picosecond (ps) timescale, lattice heating generates phonons and enables nanometalworking techniques. Later on, at the nanosecond (ns) timescale, environment heating enables applications in photothermal therapy, magnetic storage and nanorobotics. Finally, the environment cools and the cycle can repeat.

are a consequence of measuring signals at optical frequencies different from the illumination frequency; the NLO effects are essentially background free. Sensitivity is also enhanced because the NLO effects present a power-law dependence on the electric fields of light. In addition, several NLO effects are still unexplored. Within the generated higher harmonics (second, third, fourth, etc., harmonics) the emitted signal can have various origins: electric dipolar, quadrupolar, octupolar, etc., as well as magnetic dipolar, etc. The dependence of all these terms on structural, electric and magnetic properties could offer new functionalities. Within this context, plasmonic nanoparticles provide enhanced local fields in the hotspots that, in turn, can greatly enhance the detected NLO signals.[17,18] The applications of NLO effects in plasmonic nanoparticles are discussed in Section 2.1 of this review.

Within the context of plasmonic hotspots, absorption of the light into the nanoparticle generally constitutes a hindrance, as it leads to heating. However, the absorption also opens up opportunities; absorption sets off a series of processes that occur at various timescales and can have a range of useful outcomes.

Hot electrons are generated with a lifetime of up to hundreds of fs, following light absorption, see Figure 1, right panel. Hot electrons are those whose distribution can be described by the Fermi function, but with an elevated effective temperature

(up to thousands of K) compared to the rest of the material. In metals, hot electrons have a mean free path of tens of nanometers. Importantly, hot electrons were reported to be generated in greater numbers within electromagnetic hotspots.[19] Hot electrons have promising applications in energy harvesting: they generate electric current[20] and drive chemical reactions that produce fuel.[21]

The Sun irradiates 1.2×10^5 TW to the Earth.[22] The world's photovoltaic production was 5 GW in 2008, and it was 500 GW in 2018. Photovoltaic cells appear among the most promising ways to produce electrical energy at reduced carbon cost. Another attractive method is to convert solar into chemical energy by splitting water to produce hydrogen.[23] Nonradiative plasmonic decay can be useful for both solar cells and water splitting. Plasmonic materials offer several advantages: they have both large absorption cross-section and large electron density, ensuring that many photons can interact with many electrons. The solar spectrum is composed mostly of visible and near-infrared light with only 5% of the spectrum in the UV. However, semiconducting materials usually have high quantum efficiencies in the UV and visible range. Against this background, the tunable LSPR frequencies offer a range of useful electron energies to the hot electrons, covering the visible and the near IR.

In Au and Ag, plasmons generate hot electrons of 1–4 eV. Both interband (for instance between the *d* band and the conduction band) and intraband (within the conduction band) electron transitions are possible. However, the *d* band is well below the Fermi energy (at 2.4 eV and below for Au and at 4 eV and below for Ag), so intraband transitions are much more likely.[24–26] In order to use these electrons for solar cells or water splitting, they are injected into a semiconductor. The hot electrons can be harnessed by forming an interface with an n-type semiconductor (such as TiO_2, whose bandgap of 3.2 eV limits its absorption to the UV). The hot electrons with energies higher than the Schottky barrier (≈1 eV at the Au/TiO_2 interface), can be injected into the semiconductor. Electrons with energies lower than the Schottky barrier could still tunnel into the semiconductor.

After injection, the nanoparticle is left positively charged, because of electron depletion. An electron-donor needs to be in contact with the nanoparticle, to transport the generated holes to the counter electrode, keeping the charge balance and sustaining the electrical current. Hot electrons can be studied in the transient regime, using pump-probe laser experiments, which effectively freeze the clock in Figure 1. We discuss hot electrons for energy harvesting in Section 2.2.

A problem for the applications of hot electrons is that they are lost to various forms of scattering: electron–electron, electron–phonon, and electron-defects. Moreover, nanoparticles of a few tens of nm in diameter have dimensions comparable to the mean free path of the hot electrons and collisions with the surface can contribute significantly to the energy dissipation. These processes occur at a timescale of up to 5 ps and lead to lattice heating (Figure 1, bottom panel).

Photoacoustic (PA) characterization, also referred to as acousto-optic or thermoacoustic characterization, includes spectroscopic and imaging techniques, such as tomography and microscopy. Following the absorption of a photon within a nanoparticle, the rapid deposition of laser energy causes a fast (ps) heating of the environment. Due to thermodynamic expansion within that environment, the local pressure rises. The pressure then propagates as a sound wave—the photoacoustic wave—and is detected by ultrasonic transducers or microphones. The PA techniques can listen for variations of optical absorption in time, in space, and as a function of the properties of the incident light. By contrast, traditional optical techniques rely on measuring the incident, reflected, scattered and transmitted light in order to deduce absorption; a direct measurement presents obvious advantages.

Photoacoustic waves can be initiated by plasmonic nanoparticles. At the ps timescale, the hot electrons heat up the metal lattice, triggering phonon excitations. These excitations consist of longitudinal waves (similar to sound) that propagate through the lattice and beyond. Plasmonic nanoparticles are excellent frequency-tunable absorbers, and are robust in terms of optical, chemical and thermal denaturation. Moreover, for bio/medical imaging, they are biocompatible and offer easy surface functionality (by grafting on antibodies, proteins, peptides, etc.). Additionally, plasmonic nanoparticles can naturally be combined with photothermal therapies (discussed later in this review). Developments of PA imaging aim at better resolution, deeper imaging (in tissue) and higher speeds (for video rate). PA characterization is discussed in Section 3.1.

Under extreme conditions, phonons can distort and break the lattice, enabling a range of applications related to metal particle shaping at the nanoscale. *Nanometalworking* refers to the shape manipulation of metals, and related experimental techniques, at the nanoscale; it focuses on unique, size-dependent properties of metals. The thermal conductivity and the boiling point of nanoparticles are size-dependent. Nanometalworking is a major part of nanotechnology, which consists of picking up, moving and modifying nanoscale objects.[27] Specifically, nanometalworking's three main parts—forming, cutting, and joining—enable the sculpting of nanomaterials and devices. Sculpting/forming can be part of the production process, for instance when nanoparticles are brought together by chemistry and then are welded together. Sculpting can also determine the function of a material/device, for example when optical properties of a material are tuned by joining, cutting or reshaping of nanostructures. Additionally, sculpting can be part of the maintenance of a material/device, for instance when structural defects develop over time, nanometalworking techniques can be used to repair them. Just as light is used to characterize nanomaterials and devices, it is also used to sculpt or modify them.

For pulsed illumination, there are two very different regimes in nanometalworking, depending on the duration of laser pulses.[28] For continuous-wave (CW) and pulsed lasers down to the ns regime, the processes are classical and similar to those in bulk materials. They begin with the absorption of light by the metal and subsequently the heat conduction forms a spatially variable temperature profile. Depending on the achieved temperature, the materials can melt, evaporate or form plasmas. For ultrashort laser pulses (i.e., ps and fs pulses), the classical description is no longer valid and the two-temperature model provides a better description.[29] This model distinguishes between the temperature of the electrons and the temperature of the lattice. Within the duration of the ultrashort pulse, the electrons heat up, while the change in lattice temperature is negligible. Afterward, within tens of ps, the lattice heats up and the material can be transferred into a state of overheated liquid—extreme pressure, densities, and temperature build up.

On the surfaces of nanostructures, plasmonic hotspots can be literally *hot spots* useful for highly targeted nanometalworking.[30] Because plasmons constitute local field enhancements, they can locally bring the surface of a nanoparticle to a liquid state, while the rest of the nanoparticle remains solid. Therefore, plasmons offer great control, speed and energy efficiency, as well as resulting reduced costs compared to nonlocal heating. The location of plasmonic hotspots depends on the wavelength and polarization of the incident light. In Section 3.2 we discuss forming, cutting and joining at the nanoscale, all occurring at the ps timescale.

At longer timescales, up to a few ns, the environment surrounding the NP is also heated up through phonon–phonon scattering (Figure 1, left panel). This environmental heating unlocks further applications.

Nanorobotics is among the most tantalizing of future developments. Nanorobotics evokes visions of self-assembling materials, machines or even life processes. Inside the body,

1901166 (4 of 27)

**ADVANCED
SCIENCE NEWS**
www.advancedsciencenews.com

**ADVANCED
OPTICAL
MATERIALS**
www.advopticalmat.de

miniature machines are expected to perform surgery, to transport pharmaceuticals and to cooperate with bioprocesses by strengthening and repairing biostructures. Scientists are tantalized by the controlled and programmable work that biology operates at the nanoscale, throughout nature. Thus, whereas biologists aim to reverse-engineer nature, nanoscientists often proceed from first principles. The key is to efficiently transfer energy to the nanoscale and to control it, creating programmable, reusable machines that actuate rapidly and efficiently.

Various types of nanomachines have already been suggested, including nanorockets,[31,32] nanoswimmers,[33,34] nanorotors,[35–39] and nanoactuators.[40] Nanoactuation can be based on pH/ions,[41–43] hydrophobicity,[44] electric potentials,[45] and UV light-triggered systems,[42,46,47] using the *cis–trans* switch in azobenzene derivatives. One of the most promising nanoactuators is based on the temperature properties of plasmonic nanoparticles.

The actuating nanotransducers (ANTs),[48] consist of thermo-sensitive polymers—poly(*N*-isopropylacrylamide), abbreviated as pNIPAM—attached to plasmonic (gold) nanoparticles and dispersed in water. The plasmonic nanoparticles efficiently and quickly convert light into heat, triggering a strong response from the polymer. In the cold state (<32 °C), the polymer loosely binds the nanoparticles in an extended network, permeated by water. In the hot state (>32 °C), the polymer undergoes a phase transition to a hydrophobic state, causing the chains to contract and expel water. As a consequence, the plasmonic nanoparticles are brought together into a tight cluster, storing elastic energy similarly to a compressed spring. The process is highly reproducible, following the temperature cycle of illuminating plasmonic nanoparticles (Figure 1). The ANTs can exert large forces (approximately nN) in a short period of time (≤µs). Importantly, they are both water-soluble and biocompatible, which makes them suitable for biological applications.

Recent key results have demonstrated that the actuation from the ANTs can be coordinated along a common direction,[49] and that ANTs can power DNA origami constructs.[50] Moreover, the polymer can be grown within the plasmonic hotspots, in a light-guided and well-controlled fashion.[51] Additionally, some polymers are best attached to the plasmonic nanoparticles using for instance NH_2 groups (compared to SH, COOH, and H terminations); this is because the terminal group determines how close the nanoparticles are brought together in the contracted state.[52] Additionally, ANTs can serve as miniature water pumps.[53] In Section 4.1, we review these and other advances in the field of nanorobotics.

Photothermal cancer therapy based on the use of plasmonic nanoparticles is getting closer to medical reality; gold-based nanostructures have been approved by the U.S. Food and Drug Administration (FDA) as drug carriers or therapeutic agents for various phase-I clinical trials.[54,55] Gold nanoparticles offer low cytotoxicity, ease of fabrication, tunable optical properties, and an abundance of choice for surface modifications.[56] These surface modifications allow functionalization of the nanoparticles with antibodies, ligands, etc., that bind specifically to receptors on the membrane of cancer cells. This binding process is complemented by the presence of large gaps in the irregular vascular system of cancerous tissue, which leads to accumulation of gold nanoparticles.[57] The accumulated gold nanoparticles

are subsequently illuminated. Typically, near-IR laser light is used, with wavelength within the tissue transparency window (650–950 nm). When directed from outside the body, this light can penetrate usually 1–3 cm, which is sufficient for skin and breast cancers. Other cancer types can be addressed through endoscopy, whereby an optical fiber is directed inside the body to channel the laser light. The illumination and subsequent heating cause localized hyperthermia to the cancerous tissue, with little effect on the surrounding healthy tissue. The therapy has been successfully demonstrated in vivo, on several animal models (mouse, cat, and dog), and it has proceeded to clinical trials on humans.[58–63] An important limitation however is the cost of the therapy, with an estimated cost of $7500 for a single treatment.[64] In Section 4.2, we discuss medical applications of plasmonics, such as photothermal cancer therapy and plasmonic photothermal delivery of therapeutic agents.

Plasmonic steam generation is a recent development with potential applications in desalination and production of drinking water, in the sterilization of medical instruments (in areas with limited access to electricity), and in concentrating solar power (CSP) systems. In CSP systems, solar light, reflected from a large area, is directed/focused into a collector, to be converted into thermal energy. Subsequently, the thermal energy is converted into electric power using a steam turbine. For each of these applications, plasmonic nanoparticles can quickly convert solar light into heat. This ability originates from strong and tunable absorption within the region of the solar spectrum and from the limited heat capacity of the nanoparticles. As a consequence, illumination can quickly produce a vapor bubble that surrounds the nanoparticle, even though the temperature of the surrounding liquid does not rise substantially.[65]

It is important to distinguish experimental observations of water vapor from steam-based applications. Formation of water vapor can cause bubbling at the surface and can lead to condensation forming on the inside walls of containers. For most steam-based applications though, the buildup of vapor pressure is necessary. This buildup requires rising the temperature of the entire liquid, as well as thermal isolation from the surrounding environment. Plasmonic heating needs to proceed at a faster rate than the rate of cooling to the environment. The necessary sustained illumination and subsequent high temperature of the liquid should proceed without nanoparticle aggregation. Moreover, once a particle is surrounded by a bubble, its heat dissipation to the environment is strongly diminished and can lead to particle boiling. In Section 4.3, we survey recent work on plasmonic steam generation, both in the case of nanoparticles dispersed throughout the volume of the fluid and in the case of a nanostructured plasmonic surface.

Heat-assisted magnetic recording is promising for magnetic data storage with much higher storage densities than currently available. Hard disk drives are the current technology of choice for large data storage. However, the storage density is limited by the size of magnetic domains. Indeed, with decreasing domains size, the local magnetic anisotropy also decreases, which results in unstable domain magnetization over time; essentially scrambling the recording. A solution to this problem consists in using magnetic materials with very high magnetic anisotropy. Yet this leads to new problems, since the high anisotropy is then difficult to overcome by the magnetic writing

**ADVANCED
SCIENCE NEWS**
www.advancedsciencenews.com

**ADVANCED
OPTICAL
MATERIALS**
www.advopticalmat.de

head of the hard disk. Plasmonic nanoparticles can be very useful in resolving the issue. They can provide highly localized heating that is sufficient to overcome the Curie temperature of individual magnetic domains, facilitating the writing process. In Section 4.4, we briefly present heat-assisted magnetic recording.

Eventually, the environment cools back down. Upon further illumination, the cycle repeats.

2. Electromagnetic Hotspots and Hot Electrons

2.1. Nonlinear Optics

In linear optics, the electric field of light (**E**) gives rise to an induced polarization (**P**) according to the relation $\mathbf{P} = \chi^{(1)} \cdot \mathbf{E}$, where $\chi^{(1)}$ is the linear electric susceptibility. For more intense electromagnetic fields, the electrons in the material can no longer follow the frequency of **E** and the induced polarization needs to be expressed in series (or harmonics)

$$\mathbf{P} = \chi^{(1)} \cdot \mathbf{E} + \chi^{(2)} : \mathbf{EE} + \chi^{(3)} : \mathbf{EEE} + \cdots \tag{1}$$

where $\chi^{(2)}$ and $\chi^{(3)}$ are nonlinear susceptibilities for second and third harmonic generation, respectively. As it originates from the first of the nonlinear terms, the SHG is often the largest nonlinear optical (NLO) effect and it was the first to be experimentally observed.[12] SHG occurs when two photons of the same frequency annihilate to produce a single photon at twice the frequency. Within the electric dipole approximation, the nonlinear polarization at the second harmonic is written as[66]

$$P_i^{NL}(2\omega) = \chi_{ijk}^{(2)} : E_j(\omega) E_k(\omega) \tag{2}$$

where ω is the frequency of light, $\chi^{(2)}$ is the second order susceptibility tensor, $E_{i,j,k}(\omega)$ is the electric field component of the incident light, and i, j, k are the Cartesian indices.

Plasmonic enhancements of the SHG can be intuitively understood from the Lorentz model of the susceptibility, where $\chi^{(2)}$ can be expressed as a function of the resonance frequency ω_0 as[67,68]

$$\chi^{(2)}(2\omega) = \varsigma^{(2)} \frac{Ne^3}{m^2} \frac{1}{\left(\omega_0^2 - 4i\gamma\omega - 4\omega^2\right)\left(\omega_0^2 - 2i\gamma\omega - \omega^2\right)^2} \tag{3}$$

Within this equation, γ is the damping constant, N is the electronic number density, e and m are the charge and the mass of the electron, and $\varsigma^{(2)}$ is the first anharmonic term that characterizes the strength of the nonlinearity.

Similarly, for third harmonic generation (THG), three photons at the same frequency annihilate to produce a single photon at thrice the frequency. In both SHG and THG, the incident photons are processed via virtual energy states and therefore these NLO processes are considered instantaneous. Both SHG and THG scale as power-laws of the electric field of incident light and therefore they can greatly benefit from the electromagnetic hotspots generated by plasmonic nanoparticles. Moreover, SHG is a surface/interface-sensitive technique, perfectly suited to probing surface plasmons. **Figure 2** presents

four examples of nonlinear optical effects and applications that benefit from plasmonic nanoparticles.[17]

Frequency conversion is a principal application of nonlinear optics; it is used to frequency-double or to tune laser wavelengths.[69–71] Frequency conversion is advantageous in telecommunication, biology, medicine, and material science. Tuning laser wavelength requires mm-thick crystals, whose frequency conversion efficiency is weak but builds up over the length of the crystal, via phase matching. In such crystals, the frequency conversion efficiency can reach tens of percent. Tunable lasers are usually bulky and miniaturizing the technology is highly desirable.

Together with 2D materials,[72] metal surfaces/interfaces of single layer thickness,[73] are among the thinnest possible sources of SHG. However, in metal surfaces, the typical frequency conversion efficiency is of $\approx 10^{-15}$. Nanostructuring metal surfaces increases surface-to-volume ratio, which in turn increases the SHG. It also results in local field enhancements due to the lightning rod effect or to LSPRs, both boosting the SHG. There is currently an extensive toolbox for manipulating the plasmonic response, e.g., by changing the size,[74,75] the shape,[5,76] the periodicity[18] or the stacking of nanostructures.[77,78] In the case of SHG, the nonlinear response is governed by the samples' symmetry.[11] Noncentrosymmetric materials, such as GaAs are therefore good sources of SHG.
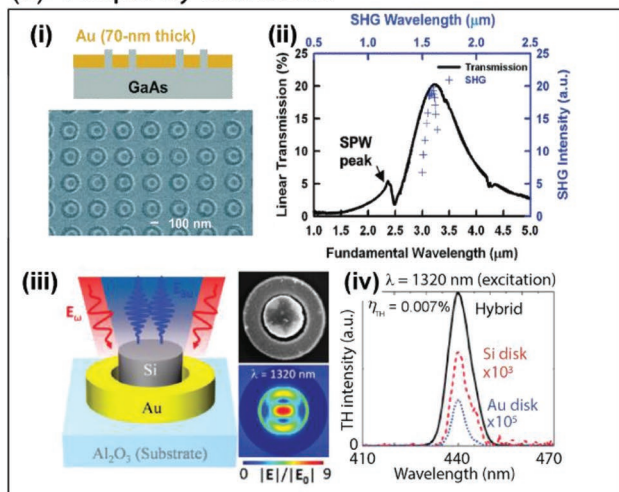
Figure 2a-i shows an array consisting of a 70 nm gold film with protrusions of GaAs. The gold serves to create plasmonic hotspots in the GaAs, thereby enhancing the frequency conversion process. Fan et al. found that such a material can strongly enhance (order of magnitude compared to the incident field) the SHG, i.e., the emission of light at twice the fundamental frequency (≈ 93 THz), over a range of frequencies (60–300 THz),[79] see Figure 2a-ii. Plasmonic enhancement also increases the THG.

Figure 2a-iii demonstrates THG from Si that is greatly increased by using plasmonic hotspots.[80] Specifically, the authors studied Si nanodisks, with a diameter of 680 nm and height of 155 nm, surrounded by a gold ring with an inner diameter of 780 nm and an outer diameter of 1360 nm. They found that the THG signal associated with this core–shell hybrid configuration was orders of magnitude larger than that of each individual structure. The spectrum shown in Figure 2a-iv demonstrates this enlargement by factors of 10^3 and 10^5 for the silicon disk and for the gold ring, respectively.[80]
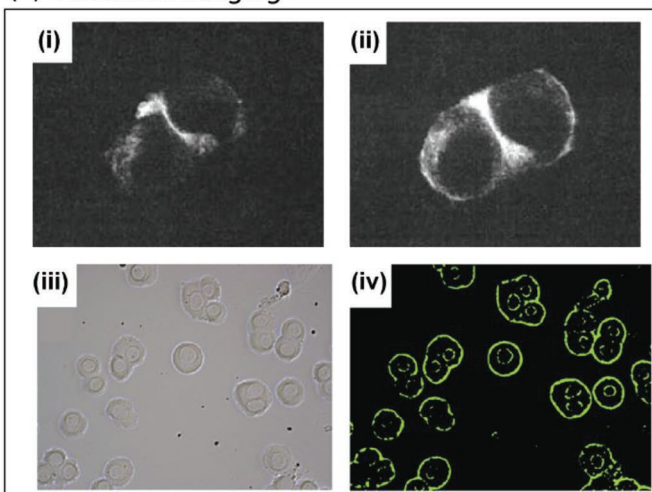
Figure 2b oversees nonlinear optical imaging with plasmonic nanoparticles. The ability to image ever smaller samples is of crucial importance in the fields of biology, physics, and medicine.[81] However, the diffraction limit of light constitutes a difficulty. The imaging resolution is expressed mathematically by the equation $d = \lambda/(2NA)$, where NA is the numerical aperture, which in optical microscopy reaches 1.4–1.6.[82,83] Depending on the wavelength λ chosen, this formula allows a resolution of the order of 0.2 μm. NLO imaging (or multiphoton microscopy) consists of illuminating the sample at λ and collecting light at $\lambda/2$ or $\lambda/3$, for SHG and THG respectively.

SHG microscopy has emerged as a powerful tool for visualization of cells and tissue structures.[84] Since SHG is essentially an instantaneous process, the use of ultrahigh repetition rate lasers allows for real-time studies in these samples.[85]
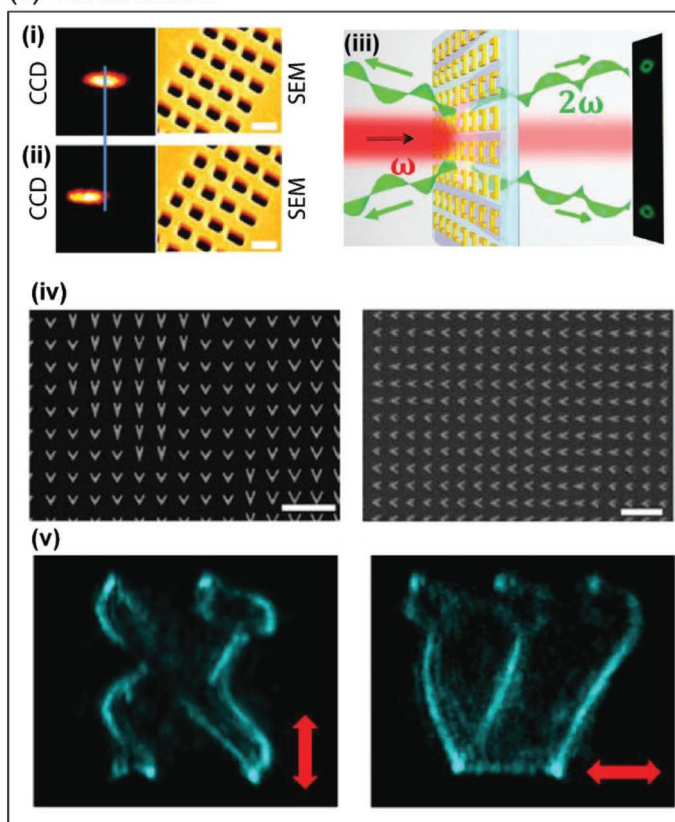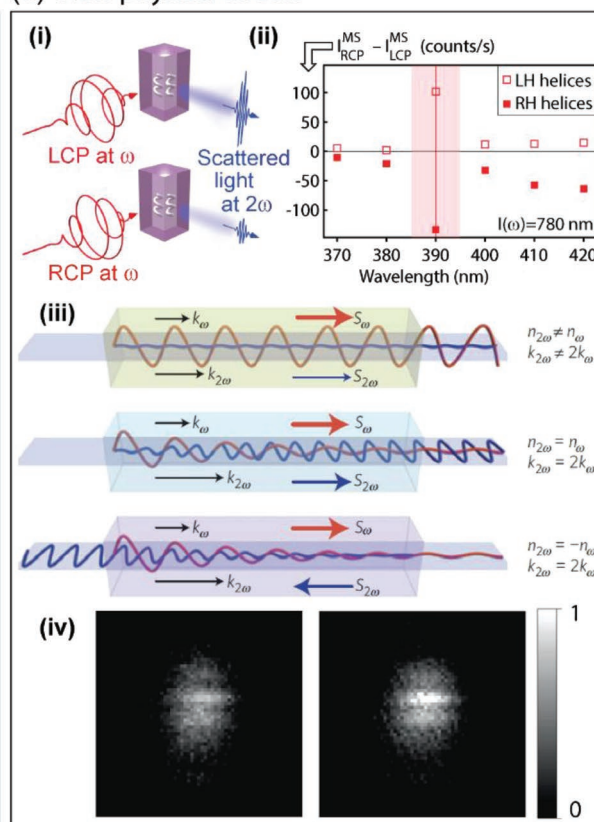
**ADVANCED
SCIENCE NEWS**

www.advancedsciencenews.com

**ADVANCED
OPTICAL
MATERIALS**

www.advopticalmat.de

Figure 2. Frontiers of nonlinear plasmonic effects. a) Frequency conversion. a-i) Schematic cross-section of structure showing GaAs annuli protruding through an Au film above an SEM image of the fabricated structure. a-ii) An FTIR linear transmission spectrum (solid black line) and wavelength-dependent second harmonic signal spectrum (blue crosses). SPW stands for surface plasmon wave. Reproduced with permission.[79] Copyright 2006, American Chemical Society. a-iii) The schematic of the experimental configuration used for THG studies. The SEM image shows the fabricated hybrid nanoantenna. The Si nanodisk has a diameter 680 nm with height 155 nm, and the Au nanoring has an inner diameter 780 nm, outer diameter 1360 nm, and height 80 nm. The simulations results show normalized electric field distribution for the hybrid. a-iv) THG spectra for the Si disk (red), Au ring (blue), and the hybrid (black), demonstrating a significant nonlinear enhancement. Reproduced with permission.[80] Copyright 2017, American Chemical Society. b) Nonlinear imaging. b-i) SHG image of N1E-115 cells prior to the addition of 30 nm gold colloids.[88] b-ii) The same cell, 30 min after the addition of the colloids. Adapted under the terms of the Creative Commons Attribution 4.0 License.[88] Copyright The Author(s), published by SPIE. b-iii) Bright-field microscopy image of anti-GPC3 antibody attached gold nanoprisms assembly conjugated human Hep G2 liver cancer cells. b-iv) The same cells, in SHG microscopy upon illumination at 1100 nm. Reprinted with permission.[91] Copyright 2016, American Chemical Society.

**ADVANCED
SCIENCE NEWS**

www.advancedsciencenews.com

**ADVANCED
OPTICAL
MATERIALS**

www.advopticalmat.de

SHG has many advantages over the well-established two-photon luminescence microscopy. There is no need for dyes/luminescent tag molecules,[86] no phototoxicity,[84] and no energy loss to the frequency conversion process.[87] However, since the two originate from fundamentally different physical processes, when SHG is used in combination with two-photon luminescence microscopy it can provide complementary information as well as insight that neither of the two techniques can grant on its own.[85] Figure 2b-i shows an SHG image of N1E-115 cells prior to the addition of 30 nm gold colloids.[88] Figure 2b-ii shows the same cell, 30 min after the addition of the colloids. A comparison demonstrates that gold nanoparticles can efficiently increase the contrast of the SHG microscopy technique. Similar enhancements can be observed for THG microscopy.[89,90] A more recent example is shown in Figure 2b-iii,iv.[91] Figure 2b-iii presents a bright-field microscopy image of anti-GPC3 antibody attached gold nanoprisms assembly on conjugated human Hep G2 liver cancer cells. The same cells are shown in Figure 2b-iv, for SHG microscopy upon illumination at 1100 nm.

Optical metasurfaces provide sharp variations to the properties of light, such as polarization, phase, direction, amplitude and frequency. These variations occur at length scales smaller than the wavelength of light. The metasurfaces are themselves made from nanoelements with dimensions and/or separating distances smaller than the wavelength of light. According to Snell's law, when a beam is incident on a medium, it will experience a change in direction depending on the direction of incidence and on the refractive index of the medium. The medium can be approximated as a series of point sources, as suggested by Huygens' principle. The phase difference between these point sources leads to constructive interferences, determining the direction of the outgoing beam. Figure 2c-i,ii shows the effects of a nonlinear metasurface.[92] In Figure 2c-i, the charged-coupled device (CCD) image shows the four-wave mixing signal from a uniform metasurface (geometry shown in scanning electron microscopy (SEM) image next to the CCD image). Clearly, the signal is centered in the image. By contrast, the signal in Figure 2c-ii is shifted. The displacement is caused by a gradient in the dimensions of the nanoarray of the metasurface, see corresponding SEM image. Because the structures are sequentially elongated along the same direction, the nonlinear phase matching conditions change.

Figure 2c-iii shows a periodic array of gold split ring resonators (SRRs), for which every second SRR is orientated in the opposite direction and each SRR is 200 nm wide.[93] By inverting the orientation of neighboring structures, it is possible to control the local phase of the metasurfaces and to cancel the zero-order diffraction of the SHG. The method provides the means to design metasurfaces particularly for nonlinear integrated optical applications.

Apart from manipulating the amplitude and the phase of light, metasurfaces can also be used to control the polarization of light. By selectively matching, or mismatching, the polarization of the incident beam with the metasurface's structure, it is possible to control whether the beam is transmitted or reflected.[94,95] Polarization control can be useful to encode polarization-dependent holograms within metasurface layers. Holograms at the SHG or THG are interesting because they are background-free.

Figure 2c-iv shows SEM images of sub-micrometer V-shaped nanoantennas, made of gold, which serve to produce THG holograms at 422 nm (fundamental at 1266 nm and 60 fs pulse).[96] The nanostructures vary in arm length and angles. Depending on the polarization of the incoming light (vertical or horizontal, as indicated with arrows in Figure 2c-v) different holograms are produced. Thus, the authors propose to design integrated nonlinear imaging solutions with high information density, as well as high resolution.

SHG and all even-order NLO effects can be highly sensitive to the symmetry breaking from the crystalline lattice,[97] to geometric field-enhancements,[98] as well as to the presence of electric[99,100] and magnetic[101,102] order. Consequently, SHG can serve to probe ferroelectric[103] and ferromagnetic[104] domains. Furthermore, SHG is exquisitely sensitive to mirror symmetry breaking: chirality.[105–107] Because plasmonic nanoparticles enhance the sources of SHG and even-order NLO processes, they can reveal previously unobserved physical effects.

Plasmonics has recently allowed the first observation of a very elusive NLO effect—Hyper Rayleigh Scattering Optical Activity (HRS OA).[108] This effect was predicted 40 years ago.[109] HRS OA refers to a difference of the scattered intensity, at the second harmonic frequency, for left and right circularly polarized illumination. This difference depends on the chirality of the scatterers (molecules or meta-molecules), see Figure 2d-i. Contrary to SHG, HRS is an incoherent process. Previous attempts to demonstrate the effect were unsuccessful. These attempts made use of helicene molecules; helicenes were excellent candidates because they combine high chiroptical response and excellent NLO properties. Nevertheless, HRS OA in helicenes and other natural molecules is generally too small to be observed directly. The effect was demonstrated for the first time using meta-molecules, i.e., nanohelices made of silver. Figure 2d-ii shows the difference in multiphoton scattering

---

c) Metasurfaces. c-i) A CCD image of the signal from a uniform metasurface unit cell. c-ii) A CCD image of the signal from a phase gradient unit cell (the scale bars in the SEM images are 500 nm). Reproduced under the terms of the Creative Commons Attribution 4.0 License.[92] Copyright 2016, The Author(s). Published by Springer Nature. c-iii) A schematic depiction of SHG diffraction from split ring resonators. Reproduced with permission.[93] Copyright 2016, American Chemical Society. c-iv) SEM images of the first and the second layer of a 3D nonlinear hologram (scale bar is 1 μm). c-v) The projected holographic images of the Hebrew letters Alef and Shin for vertically or horizontally polarized input beams, respectively. Reproduced under the terms of the Creative Commons Attribution 4.0 License.[96] Copyright 2016, The Author(s). Published by Springer Nature. d) New physical effects. d-i) A schematic diagram of the Hyper-Rayleigh Scattering Optical Activity effect (HRS OA). d-ii) Experimental results demonstrating the HRS OA effect, for the first time. Upon illumination at 780 nm, the difference in multiphoton scattering, for left and right circularly polarized light, is very large at 390 nm, and it reverses with the chirality of the nanostructures. Reproduced under the terms of the Creative Commons Attribution 4.0 License.[108] Copyright 2019, The Author(s). Published by the American Physical Society. d-iii) Schematic diagram of the nonlinear mirror effect. d-iv) Experimental results demonstrating the nonlinear mirror effect, for the first time. The images show SHG signal, where the appearance of back-propagating SHG (on the right) is controlled with an applied electric signal. Reproduced with permission.[110] Copyright 2015, Springer Nature.

(MS) with left and right circularly polarized light, $I_{RCP}^{MS} - I_{LCP}^{MS}$, at 780 nm. At 390 nm, there is a very large difference in this scattering, which reverses with the chirality of the nanostructures, as expected of optical activity. HRS OA has been estimated to be at least 100 000 times more sensitive than linear optical activity and could find applications in ultrasensitive characterization of chiral molecules and pharmaceuticals.

Similarly, Figure 2d-iii presents a physical effect that had been predicted 10 years earlier, and whose observation was made possible by advances in plasmonics.[110] In bulk materials, second harmonic light can be generated along the propagation direction but it usually cancels out due to destructive interference. By contrast, in the so-called "phase-matched" materials, the second harmonic light builds up along the propagation direction of the fundamental beam, following constructive interference. An interesting behavior can be observed in phase-matched materials with negative refractive index. In this case, the SHG counter-propagates with respect to the incident beam, and the phenomenon is referred to as "backward phase-matching" or "nonlinear mirror." Figure 2d-iv demonstrates SHG intensity that is intrinsic to the materials (left) and SHG intensity that is attributable to the nonlinear mirror (right), where the latter was controlled by E-FISH (electric field induced second harmonic generation).

2.2. Hot Electrons

In Figure 1, we described a situation where photons incident upon a metal NP excite surface plasmons. The plasmons can lose their energy by either radiating a photon, or creating an energetic, or "hot," electron–hole pair. The latter process is known as Landau damping; under the effect of the electric field produced by the surface plasmon resonance, intraband and interband electron transitions occur in the metal.[111] The process is nonradiative and occurs on a timescale of up to 100 fs. These hot electrons are electrons from below the Fermi level of the NP, which, by absorbing the energy of the incident light hf, have been promoted into states that lie high above the Fermi level. The process can be described by the two-temperature model (TTM). Starting with the heat equation, which describes the diffusion of heat in a system, the model consists of writing two such equations: one for the temperature of the electron gas at time t and at coordinate r, i.e., $T_e(r,t)$, and one for the temperature of the ion lattice $T_l(r,t)$. In the TTM, these differential equations are coupled by the electron–phonon coupling constant (G):

$$C_e \frac{\partial T_e(\boldsymbol{r},t)}{\partial t} = K_e \Delta T_e(\boldsymbol{r},t) - G\left[T_e(\boldsymbol{r},t) - T_l(\boldsymbol{r},t)\right] + S_1(\boldsymbol{r},t) \quad (4)$$

$$C_l \frac{\partial T_l(\boldsymbol{r},t)}{\partial t} = K_l \Delta T_l(\boldsymbol{r},t) - G\left[T_l(\boldsymbol{r},t) - T_e(\boldsymbol{r},t)\right] + S_2(\boldsymbol{r},t) \quad (5)$$

C and K are the heat capacities and thermal conductivities of the electrons and of the ion lattice, indicated with subscripts e and l, respectively (and assumed constant for simplicity of the notations). $S_1(r,t)$ is a source term that represents the laser energy deposition per unit area and unit time. $S_2(r,t)$ is also an energy source term that is often neglected since light interacts mainly with the electrons of the material. Moreover, the lattice heat conductivity is often negligible in comparison to the electron heat conduction in metals.

Within this model, light initially creates nonthermalized electrons. Following electron–electron interactions, the electron population thermalizes, i.e., an effective temperature can be assigned to the distribution of the electron energies. The energy of the electrons is subsequently transferred to the lattice via G. Eventually, T_e and T_l reach equilibrium.

In metal nanoparticles, the source term $S_1(r,t)$ depends on the photon flux and on the absorption cross section of the metal NPs.[112] The latter depends directly on the surface plasmon resonances. In turn, the NP dielectric function changes value due to the ultrafast perturbation of the electron distribution.[113]

The simple TTM model can be extended in various ways. For instance by including dependencies of the heat capacities and thermal conductivities on the temperatures of the electrons and lattice.[114] It can also separate between the thermalized and nonthermalized electrons,[115] and include surface and grain boundary scattering.[116]

Hot electrons could be useful in many applications such as optoelectronic devices,[117] renewable energy,[7] and catalysis.[76,118] However, the application of hot electrons in real life is hindered by their short lifetime, on the order of hundreds of fs on most surfaces.[119] This hurdle can be overcome by exploiting plasmonic NPs to generate hot electrons, thanks to their extended carrier lifetimes and discretized energy levels.[120] In this section, we review some of the recent advances in the fields of catalysis and photovoltaic devices based on hot electrons.

2.2.1. Catalysis

Plasmonic NPs are excellent candidates for performing plasmon-enhanced photochemistry thanks to their ability to absorb and scatter light from a broad range of the electromagnetic spectrum.[121] This capability is in stark contrast with traditional semiconducting photocatalytic materials, like TiO_2,[122–125] where the absorption spectrum is determined strictly by the bandgap of the material. In the case of TiO_2, whose bandgap is 3.2 eV,[126] the absorption is in the UV,[122] which covers only ≈ 5% of the solar spectrum—a major limitation to the efficiency of TiO_2 for renewable energy applications. Therefore, the discovery that plasmonic metal NPs can greatly outperform traditional semiconductor photocatalysts has led to a step-change in the field of photocatalysis and a surge in publications (see refs. [7,76,127–129] for recent reviews). A vibrant new direction of this field, which has also been subject to much debate over the last decade, is the role of hot electrons in plasmon-enhanced catalysis.

There are three main pathways along which plasmon-enhanced catalytic reactions can proceed. The first is referred to as conventional photochemical catalysis and involves reactions where a certain photosensitive material requires the presence of light to proceed, e.g., polymerizations.[130] In this situation, it is straightforward to recognize the benefit of using plasmonic NPs due to their ability to strongly enhance the optical near

**ADVANCED
SCIENCE NEWS**
www.advancedsciencenews.com

**ADVANCED
OPTICAL
MATERIALS**
www.advopticalmat.de

field.[131,132] The second catalytic mechanism involves heat. In general, the rate K_R of chemical reactions depends exponentially on temperature, following an Arrhenius-type relationship ($K_R \propto$ exp ($-E_a/k_B T$), with E_a the activation energy of the reaction, K_B Boltzmann's constant, and T the absolute temperature). Therefore, being able to provide a light-controlled localized heating mechanism makes plasmonic NPs ideal for applications that require low-power operation or fast heating dynamics. The third catalytic mechanism involves the excitation of molecules near plasmonic NPs via hot electrons. This mechanism is nonthermal in its origin as it involves the capture of hot electrons, generated in the first step of the plasmon relaxation described in Figure 1, before they could thermalize with the lattice. This mechanism is possible because the hot electrons have a higher energy than equilibrium electrons and can effectively spill out of the NP and populate the unoccupied molecular orbital of a nearby molecule. At this point a concentration of negative ions is created that subsequently evolves naturally and may result in desorption, diffusion, or dissociation of the targeted molecule. A rigorous theoretical study suggests that plasmonic NPs could improve catalysis in this manner.[3]

In many catalytic systems, the enhanced chemical reactivity arises because of the synergy between a thermal and a nonthermal reaction pathway. Disentangling one from the other is nontrivial and has therefore become a subject of debate in literature. Examples of hot-electron assisted catalysis include the dissociation of H_2 on Au NPs,[21,133] water splitting with visible light on a TiO$_2$ substrate[23] and on a Au nanorod array,[134] and the oxygen dissociation[135] and oxidation of ethylene on Ag nanocubes.[136] In the first example, Mukherjee and colleagues were first able to dissociate H_2 and D_2 on a TiO$_2$ substrate covered with Au NPs, thereby forming HD molecules.[21] By later repeating the experiment on a SiO$_2$ substrate, they showed that the reaction was enhanced even further, pointing to a mechanism whereby the catalysis happens on the surface of the Au NPs, rather than on the substrate. More specifically, the authors describe the catalytic mechanism in several consecutive steps: the matrix of TiO$_2$ increases the dwell time of the hydrogen molecules near the gold surface. This enhances the efficiency of population of the antibonding state by the hot electrons generated in the NPs. Populating the antibonding state leads to the hydrogen molecule becoming a negative ion, called the transient negative ion by the authors. As in small NPs the excited hot electrons live longer than in a substrate, they have longer time to interact with the transient negative ions, traveling around the excited NPs. This creates conditions for more efficient extension of the bond length of the ion, which eventually results in dissociation. Mukherjee and colleagues conclude that the photocatalytic process of dissociation, taking place at room temperature is thus only accomplished by the hot electrons generated by the small AuNPs, without applying heat or other external sources of energy. A comparison between the spectral response of the reaction rate and the extinction spectrum of the Au NPs also showed a remarkable similarity. The authors thus concluded that the catalysis proceeded by the conversion of a single photon into a single hot electron which triggered a single H_2 dissociation event.[133]

Along similar lines, in the case of light-induced water splitting on a TiO$_2$ substrate, a 66-fold increase in the reaction rate with the addition of Au NPs to the TiO$_2$ substrate was attributed to the near-field enhancement of the generation of hot electron–hole pairs on the substrate surface.[23] Most significantly, Christopher et al. were able to identify a clear footprint of electron mediated catalysis by studying the reaction rate of ethylene oxidation on Ag nanocubes as a function of incident light power and temperature.[136] The authors observed a clear transition from a linear to a power-law rate dependence on light intensity (i.e., rate $\propto$ intensity^n, with $n > 1$), which is an indicative sign of an electron driven chemical reaction. The authors explain the dissociation of the molecular oxygen by the population of the unoccupied orbitals by energetic electrons, during the relaxation of the light-excited localized surface plasmon resonance. This electron-driven dissociation takes place at the surface of Ag in both regimes—for linear and power-law dependence. Moreover, the group showed that the quantum efficiency (reaction rate divided by rate of impinging photons) of the reaction increased with light intensity and with temperature, contrasting the behavior of conventional semiconductor photocatalysts.[136]

A new approach to exploiting hot electrons as photocatalysis drivers is the design of bimetallic nanostructures. In this case, the aim is to create NPs with a plasmonic core that converts light into energetic electrons and a catalytically active shell.[137] A recent example of purely electron driven nonthermal catalysis with such core–shell structures was demonstrated by Ortiz et al., who used Pt end-capped Au nanorods for the efficient production of hydrogen using white light.[138] Similar core–shell nanostructures have been used extensively over the last five years to catalyze a wide variety of chemical reactions.[118,139–143] However, the exact mechanism that underpins the catalytic reaction (thermal or nonthermal) has proven to be specific to each system. For example, when AuPd bimetallic nanostructures were used to catalyze the reaction rate of hydrogenation[141] and the yield of a set of Suzuki reactions,[142] it was identified that the role of the electronic mechanism was overshadowed by that of photothermal heating, occurring after the hot electron population has thermalized with the lattice. By introducing a 25 nm thick layer of TiO$_x$ in between the Au core and the Pd caps, the authors were able to prevent the electrons from spreading from the Au core into the Pd caps. This resourceful approach reveals the physics behind the observed plasmon-enhanced catalytic efficiency and helps to identify the electronic contribution, whilst still observing enhancement in the reaction yields due to the simple heating. This result provides support for both the purely photothermal catalytic mechanism in the presence of the separating TiO$_x$ layer and for the combined effect of photothermal conversion and plasmonic photocatalysis without the TiO$_x$ layer.[142] In the latter case, the yield of the Suzuki coupling was improved approximately twice compared to the former case under the same illumination conditions, thus assessing the individual contribution of the nonthermal processes in the specific system presented. Therefore, it is apparent that both heat and light can play a role in these reactions, as also illustrated in ref. [143].

With a Rh/TiO$_2$ catalyst, initially, the thermal reaction rate is dominant. For higher illumination intensity though, a nonthermal rate can be observed, whose efficiency grows with a power-law dependence on the illumination intensity. By

contrast, Ranno et al. performed a theoretical study on core–shell nanostructures for water splitting reactions, which require both hot electrons and hot holes in order to proceed.[3] By considering different combinations of alkali metals and transition metals, they were able to show that alkali metals produce more hot electrons than transition metals. The authors attribute the calculated improved efficiency of these bimetallic NPs to the predominant generation of hot carriers at the surface, in the NP tiny shell, from where their extraction is more efficient and present a confirmation, based on the case of K-core/Au-shell nanoparticle. The authors were also able to show that NPs comprising a combination of both types of metals, in particular K on Au and Na on Au, are the best candidates for catalyzing water-splitting reactions. Moreover, this result was supported by a direct comparison with monometallic NPs. In addition, the authors looked into the catalytic ability of core–shell NPs as a function of their core size at a fixed total outer diameter. The authors concluded that NPs smaller than 4 nm in diameter produce fewer hot electrons per unit volume, with the hot carrier generation rate at its peak for NPs of 5 nm diameter.[3] The authors pointed out that the physics behind that theoretically predicted phenomenon is related to the change that takes place in the energy levels of the NPs as their diameter is increased. The authors calculate that for an NP radius less than 4 nm, discrete energy levels occur and the spacing between the levels gradually shrinks with increasing radius. The number of the generated hot carriers also increases with radius, with a maximum calculated to be around the radius of 5 nm. The calculations show that further increasing the NP radius leads to generation of lower energy carriers that are of lower catalytic efficiency.

2.2.2. Solar Cells and Photodetection

Apart from catalyzing chemical reactions, hot carriers generated in plasmonic materials can also be used to improve the efficiency of solar cells and in photodetection.

The efficiency of solar cells is strongly linked to their absorption. For example, for the wide-spread solar cells made of Si, the absorption is limited by the fact that Si has an indirect bandgap. Si solar cells therefore have to be thick in order to maximize absorption.[111] However, when the thickness of the active zone is increased, the efficiency of collecting the generated electron–hole pairs decreases, because some of the free carriers recombine on route to the collection electrode.

The absorption of light by materials is also wavelength dependent. Around 50% of solar photons have a wavelength in the interval 780–2500 nm.[144] However, Si has a higher quantum efficiency in the visible region and only absorbs wavelengths below 1100 nm.[144]

Plasmonic materials can enhance the performance of solar cells through scattering (light trapping), hot carrier generation, and plasmon-induced resonance energy transfer (PIRET).[145] Scattering increases the travelling length of light in the solar cell, thus increasing absorption. Hot carriers are generated in plasmonic materials through Landau damping—the plasmonic decay into hot electron–hole pairs. When the plasmonic material is placed in contact with a semiconductor, the hot carriers

are injected into the semiconductor, provided that their energy is high enough to overcome the Schottky barrier at the interface. Thus, free electrons (or holes) are created in the conduction (or valence) band of the semiconductor. However, unlike standard solar cells, where the carriers are created through absorption in the semiconductor, the absorption appears in the plasmonic material; this process offers high absorbance at wavelengths of choice.[24] Specifically, by tuning the shape of plasmonic NPs, it is possible to shift the absorption maximum of the solar cell toward the IR, where the solar spectrum is rich in photons.[144] The third enhancement mechanism mentioned above, PIRET, is an energy transfer between a plasmonic metal and a semiconductor via dipole-dipole or multipolar coupling.[145,146] Below we provide a few examples of these physical mechanisms.

Baek et al. designed Au–Ag core–shell nanocubes which they embedded in an anodic buffer layer of an organic solar cell.[147] The Au–Ag nanocubes acted as scatterers and the power conversion efficiency of the solar cells was improved by up to 18%.

Liu et al. made use of the hot electron generation properties of plasmonic materials to improve performance of Si-based solar cells.[144] The authors created monocrystalline Si nanowire arrays with Ag nanoplates. Hot electrons were generated in the Ag nanoplates and were injected into the Si nanowires. The authors reported that the external quantum efficiency of their device was enhanced by 59% for incident light of 800 nm wavelength thanks to the integration of the Ag nanoplates.

Li et al. investigated PIRET in $Au/SiO_2/CuO_2$ core–shell NPs.[146] The wavelength range of the absorption of the NPs was wider than for the semiconductor (CuO_2) alone as PIRET resulted in charge carriers being created even when the NPs were irradiated with energies below the bandgap of CuO_2. The authors reported that the number of carriers created in CuO_2 when irradiated with 650 nm light was ≈1.4 times higher than that for light with above bandgap wavelength of the same incident flux.

Similarly to solar cells, semiconductor-based photodetectors work on the principle of converting light to photocurrent. Therefore, the capabilities of photodetectors can also be enhanced by the mechanisms listed above, especially through hot carrier generation.[148–152] Such photodetectors can even detect light below the semiconductor's band edge which might allow Si-based devices to be used for detection at telecommunication wavelengths.[148,149,151]

For more information about plasmonics applied to photovoltaics and more generally plasmonic metal/semiconductor interfaces, the reader is referred to the reviews in refs. [111,145,153,154].

3. Heating up the Lattice

In Figure 1, following the generation of hot electrons, the lattice heats up and phonons are generated. This process is often described by the two temperature model, presented in the previous section. In Equations (4) and (5), it is the electron-phonon coupling constant (G) that is responsible for heating up the lattice. In bulk gold, $G \approx 3 \times 10^{16}$ W m^{-3} K^{-1} S^{-1} and in bulk silver $G \approx 3.5 \times 10^{16}$ W m^{-3} K^{-1} S^{-1}.[155] With fs laser pulses, the

energy transfer from the hot electrons to the lattice phonons is of the order of several ps.[156] For spherical plasmonic nanoparticles, the transfer of energy can be considered homogeneous and isotropic, which causes the nanoparticles to expand. The expansion sets up a radial vibrational mode, known as the "breathing mode."[157] The period of oscillation T is proportional to the radius of the nanoparticles (R):[158,159] $T_{br}^{(n)} = (2\pi R)/(\chi_n c_l)$, where c_l is the longitudinal speed of sound and χ_n is an eigenvalue from $\chi_n \cot \chi_n = 1 - (\chi_n c_l)/(2c_t)^2$, with c_t being the transverse speed of sound.[160] For Au nanoparticles that are 40 nm in diameter (and larger), the period of oscillation is of the order of tens of ps.[161] This motion can be described as a damped harmonic oscillation, where the damping term represents heat loss to the environment of the nanoparticle. In turn, the lattice vibrations can give rise to acoustic waves.

3.1. Photoacoustics

Following the absorption of light in plasmonic nanoparticles, at the ps timescale, electrons lose energy due to electron-lattice collisions. In the process, phonons are created. The word "phonon" derives from the Greek word for sound or voice, since phonons can produce sound waves. A phonon is defined as the quantum or quasiparticle associated with the collective excitation of lattice vibrations.[162] The frequencies of the propagating wave are split into an upper (or "optical") branch and a lower (or "acoustic") branch. Optical phonons arise from slight differences in the charge distribution of two neighboring atoms in the lattice. This difference in charge creates an effective dipole that interacts with electromagnetic waves, typically in the infrared spectrum.[162] In plasmonic nanoparticles, there are two main types of phonon modes: the radial (or breathing) mode and the longitudinal (or "extensional") mode.[163]

The lattice dynamics can therefore be studied with optical techniques, as has been shown by Del Fatti et al., who used two time-delayed fs pulsed laser sources in a pump-probe scheme to investigate Ag thin films (23 nm) and nanoparticles (13 nm) both submerged in a glass environment.[164] The authors excited the phonons around the plasmon resonance frequency in both cases and measured the change in transmission. Their technique was able to show the typical timescales associated with electron-lattice collisions (i.e., < 1 ps) as well as to confirm that the probed mode was indeed the acoustic mode, due to vibrations of much longer lifetime. The authors further suggest that the changes of the electronic properties observed are a direct consequence of the changes of the real part of the dielectric function of the material induced by the lattice vibration.

Zijlestra et al. studied single gold nanorods with an average length of 90 nm and width of 30 nm.[165] They showed that by combining scanning electron microscopy image characterization with scattered light spectroscopy and a 300 fs Ti:sapphire laser at 800 nm, it is possible to determine the elastic moduli of gold nanorods. The nanorods exhibit both the breathing and the extensional mode. The authors demonstrate that, in some cases, the elastic moduli of the nanorods are in good agreement with that of the bulk. Consequently, this technique offers a way to investigate the scales at which elastic properties of materials start to differ.

Since light-induced lattice dynamics are intrinsically linked to electron-lattice collisions (acoustic mode), it is possible to measure the phonons using plasmonics. Soavi et al. showed this for gold nanorods with 20 nm height, 30 nm width and lengths varying between 70 and 200 nm. The authors used pump-probe spectroscopy to quantitatively study the extensional mechanical oscillations of macroscopic arrays of gold nanorods. They were able to follow the mechanical elongation of the nanorods in real-time, by measuring the transient shift of the LSPRs. Their technique was sensitive to nanorod oscillations with amplitude down to 0.25 pm.[163]

Thijssen et al. studied plasmon-mechanical coupling in nanomechanical oscillators made from two elongated nanorods. The nanorods were made of silicon nitride and were either metalized with gold or supported gold nanoantennas, with a gap size of 25 nm and 30 nm respectively.[166,167] The results show that, at the plasmon resonance, the thermally driven motion of the two nanorods corresponds to the vibrational modes probed when the sample is measured in a vacuum chamber. Both the breathing and extensional modes were probed by measuring the spectral density of the transmitted light. This technique allows the authors to measure phonons with a frequency of up to 10 MHz, as well as to study the effect of changing the illumination wavelength and the gap size. These nanomechanical oscillators could serve as sensors for tiny forces.

If sufficiently large, lattice vibrations can compress air in a small volume surrounding the material, resulting in the emission of sound waves that can be detected using microphones. These sound waves can be interpreted as an echo of the phonon and are useful to study how the absorbed energy is distributed in a lattice—a field known as photoacoustics.

Photoacoustic imaging was proposed in 2001 by Oraevski et al.[168] It has since emerged as a strong candidate for noninvasive imaging and can be divided into two techniques—photoacoustic tomography and photoacoustic microscopy.[169] In 2004, Wang et al. proposed to use gold-silica nanoshells with a thickness of 10–12 nm and an optical absorption peak at about 800 nm as a contrast agent for photoacoustic measurements of in vivo rat brains. Gold was used because of its biochemical inertness and because it offers a high degree of control for constructing self-assembled monolayers in the presence of certain polymers, such as polyethylene glycol. The process benefits from the fact that optical absorption in gold nanoparticles can be controlled by changing their shape and dimensions. The authors used a pulsed, tunable dye laser at 800 nm to illuminate the top of an immobilized rat's head, which was submerged in a water tank. A transducer in the water tank was used to measure the photoacoustic waves around the rat's head to construct a cross-sectional photoacoustic tomography image of the brain.

Later Zhang et al. showed that gold nanorods can be stabilized in a similar fashion with polyethylene glycol and were able to image cancerous tumors in living rats, in air.[170] Gold nanoshell assemblies were found to accumulate in melanomas,[171] macrophages associated with plagues[172] and tumor tissue.[173] While these studies show the great potential of gold nanoparticles for photoacoustic imaging, the potential toxicity of gold nanoparticles is yet to be sufficiently investigated and is actively researched at the moment. A recent review giving a

detailed overview over the potential of gold nanoparticles for bioimaging and sensing can be found in ref. [174].

When light interacts with plasmonic nanomaterials, it can be transmitted, reflected, scattered or absorbed. There are various ways to measure transmitted, reflected and scattered light. These measurements usually serve to derive the intensity of absorbed light. Recently, Belardini et al. employed photoacoustic techniques to directly measure the intensity of absorbed light in gold nanowires,[175] chiral platinum-gallium-carbon nanohelices,[176] in self-assembled GaAs nanowires[177] and in chiral metal-polystyrene metasurfaces.[178] Upon absorption in the samples, light causes local heating, which is transferred to the small volume of air surrounding the sample, creating a pressure wave. Modulating the incident light intensity (with an optical chopper) translates in acoustic pressure modulation, at the same frequency. The acoustic signal is then collected with a microphone and translated into electrical signal. This photoacoustic technique is particularly important for studying chiral nanoparticles, because the chiroptical response in absorption can have an opposite sign to that in scattering.[179]

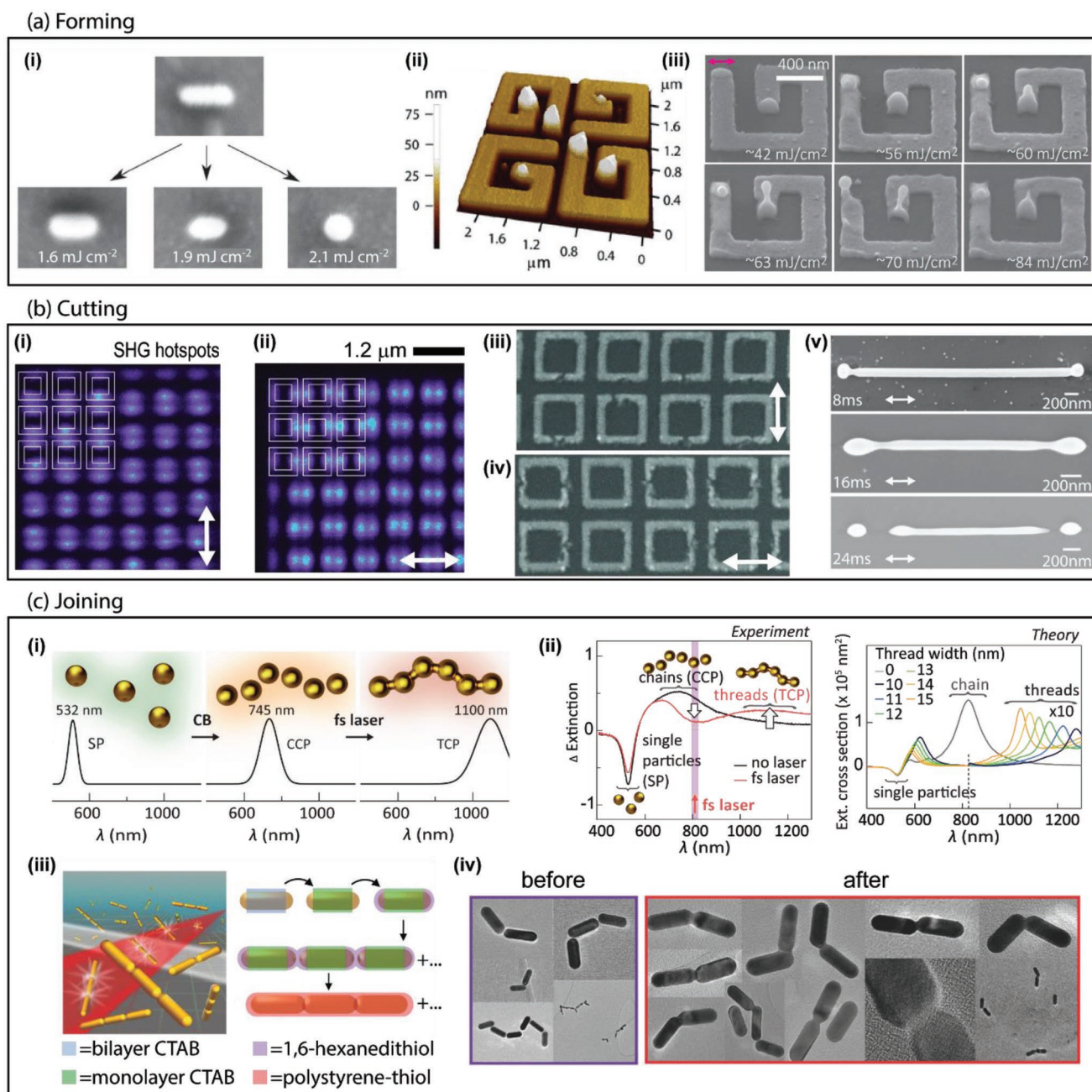## 3.2. Nanometalworking: Ablation and Related Effects

Metalworking can be divided into three types—*metal forming, cutting, and joining*. All three can be performed at the nanoscale with lasers, via one of two main physical mechanisms. The first mechanism is the classical heating of bulk materials, which consists of progressively rising temperature, until the melting and boiling points are reached. This process takes place for CW or pulsed lasers, down to the ns pulse duration. The other physical mechanism occurs for shorter laser pulses (e.g., ps and fs). Over these very brief periods of time, the light energy is absorbed by the electrons but the lattice remains cool. Energy transfer to the lattice occurs subsequently, within tens to hundreds of picoseconds,[180] a process known as "ablation." The lattice can then melt, begin to evaporate or fragment into smaller pieces.[181] Ultrafast laser pulses are usually focused with microscope objectives for maximum peak-power per unit area. In continuous gold films, the ablation threshold is achieved for laser fluence of 0.4 to 1.4 J cm^{-2}, using 100 fs pulses.[182,183]

In nanostructures, because the physical dimensions are smaller than the optical penetration depth, it was initially reported that the temperature is almost homogeneous over the entire volume of the nanostructure.[184] Melting was reported to follow surface tension rules, starting with the sharpest edges and proceeding to form spheres. Inhomogeneous temperature distribution over the volume of the nanoparticles was then first revealed,[30] highlighting the role of optical near-fields. These fields can be highly inhomogeneous at the surface of nanostructures. Indeed, the incident light pulses cause oscillations of the surface electron density and, depending on the polarization of light and on the geometry of the nanostructures, high-electron-density regions are created—the hotspots. These hotspots offer high spatial control and enable precise targeting of the ablation process.[185–188] Moreover, they lower the thresholds for ablation;[29,30,189] e.g., down to 9 mJ cm^{-2} in the case of electromagnetic enhancements from sharp edges.[190]

Figure 3a demonstrates extremely high control over the location and the shape of material forming at the nanoscale. Figure 3a-i shows SEM images of gold nanorods (92 nm × 30 nm), upon illumination with 100 fs laser light at 750 nm, i.e., at resonance with the longitudinal LSPR.[191] The nanorods progressively change shape, depending on the fluence of the laser; a perfect sphere can be observed at 2.1 mJ cm^{-2}. In this example, the entire nanostructure is transformed. By contrast, the atomic force microscopy (AFM) image in Figure 2a-ii presents a case where only a part of the nanostructure is reshaped.[192] In this image, the hotspots are marked with localized material overgrowths (following reshaping), while the rest of the nanostructures are clearly unaffected. These overgrowths were formed following illumination with millions of light pulses. In order to elucidate the exact process of their formation, the experiment was repeated for single pulse illumination, upon varying the pulse energy. The results are shown in Figure 3a-iii, where each SEM image corresponds to nanostructures that have been illuminated with different light pulse energies. The arrow indicates the direction of light polarization. Initially, a nanobump is formed in the hotspots.[193] For higher pulse energy, the nanobump evolves in a nanoscale jet formation (nanojet). It can be seen that the nanobumps are hollow—material from the hotspot region is used to form a spherical droplet that rises and eventually detaches from the hotspot region. The physical process is akin to throwing a pebble in a pool of water and observing the liquid back-jet, followed by droplet projection. For the experiments in Figure 3a-iii, the plasmonic effect lowered the ablation threshold to 2.7 mJ cm^{-2}. Similar material deformations were subsequently observed in simpler geometries, i.e., nanostripes with varying lengths.[194]

Figure 3b shows how electromagnetic hotspots can precisely mark the location of light-induced cuts to metal nanostructures. In continuous metal films, metal cutting with laser ablation is well-known.[195,196] Figure 3b-i shows an SHG microscopy image from square-ring nanostructures, made of gold.[197] The geometry of the nanostructures is shown in a white overlay. Laser illumination (800 nm, 100 fs, at 82 MHz light pulses) with vertical polarization (indicated as a white arrow) reveals the location of SHG sources, corresponding to the electromagnetic hotspots. The location of these hotspots changes with the direction of the polarization, as demonstrated in Figure 3b-ii. Upon increasing the laser intensity above the ablation threshold, the square-rings are cut in the locations of electromagnetic hotspots, as shown in Figure 3b-iii,iv, for vertical and horizontal light polarization, respectively. Another example of cutting a nanostructure with fs laser light is presented in Figure 3b-v.[198] The SEM images display silver nanowires (≈2150 nm × ≈80 nm), irradiated with laser fluence of ≈130 mJ/cm^{-2}, for different lengths of time; the direction of light polarization is indicated with white arrows. After 24 ms illumination, the nanowire is cut into three parts, though the shape of the entire wire is affected.

Just as lasers can cut nanostructures, they can also join/weld them together. Figure 3c-i presents three distinct optical resonances associated with gold nanoparticles, which can be used to follow the process in real-time.[199] The single nanoparticle plasmon resonance (SP) is situated at 532 nm. Using molecular linkers, these nanoparticles can be assembled into chains

ADVANCED
SCIENCE NEWS
www.advancedsciencenews.com

ADVANCED
OPTICAL
MATERIALS
www.advopticalmat.de

Figure 3. Nanometalworking with light—forming, cutting, and joining. In (a), forming is presented. In (a-i), an illuminated nanorod can be reshaped into a perfect sphere. Adapted with permission.[191] Copyright 2009, the Royal Society of Chemistry. In (a-ii), targeted reshaping is demonstrated, only in the electromagnetic hotspots, while the rest of the nanostructures are unaffected by the illumination. The AFM image is of gold G-shaped chiral arrays. Reproduced with permission.[192] Copyright 2018, the American Physical Society. In (a-iii), single fs pulses produce nanojets from the electromagnetic hotspots. Scanning electron microscopy (SEM) of the G-shaped nanostructures reveals the evolution of a nanojet formation with increasing illumination fluence. The direction of light polarization is indicated with the pink arrow. Reproduced with permission.[193] Copyright 2012, Wiley-VCH. In (b), examples of laser cutting are shown. b-i,ii) SHG microscopy images of hotspots induced by light with vertical and horizontal polarization, respectively, in square-shaped gold nanostructures. b-iii,iv) SEM images of the sample arrays after illumination with fs pulsed light, polarized vertically and horizontally, respectively. The locations of the cuts match the hotspots' locations. Reproduced with permission.[197] Copyright 2012, Wiley-VCH. In (b-v), the SEM images display silver nanowires (≈ 2150 nm × ≈ 80 nm), irradiated with laser fluence of ≈130 mJ cm^{-2}, for different times; the direction of light polarization is indicated with white arrows. After 24 ms illumination, the nanowire is cut into three parts, though the shape of the entire wire is affected. Reproduced with permission.[198] Copyright 2016, IOP Publishing. In (c), two examples of metal joining are shown. c-i) Three plasmonic resonances: single particle (SP), capacitive chain plasmon (CCP), and threaded chain plasmon (TCP). Chains are linked by cucurbit-uril (CB) molecules. c-ii) Differential extinction spectra (normalized at the spectra of single NPs in solution), upon introducing CB, with (red) and without (black) laser illumination. Numerical simulations of resonant six-NP-long chains display TCP mode and indicate the range of nanothread widths contributing to the signal in the experimental data. Reproduced under the terms of the Creative Commons Attribution 4.0 License.[199] Copyright 2014, The author(s). Published by Springer Nature. c-iii) Schematic of the plasmonic nanoantenna formation process. In (c-iv), the purple and red boxes present TEM images before and after welding, respectively. Adapted with permission.[200] Copyright 2017, Wiley-VCH.

whose characteristic chain plasmon resonance is observed at 745 nm. Upon illumination with an ultrafast laser, with fluence above the ablation threshold, the nanoparticles are welded together and fixed in position; as if on a metal thread. The welded chains of nanoparticles exhibit a characteristic resonance at 1100 nm. In Figure 3c-ii, this distinct plasmon resonance can be seen at work. In the experimental data, the black curve presents a dip at 532 nm, due to a diminishing number of single nanoparticles, as they are bound into chains by the linker molecules. Correspondingly, there is a peak at 745 nm. The red trace corresponds to data from conducting the experiment in the presence of ultrafast laser light at 800 nm (100 fs, 1 kHz). Again, a dip can be seen at 532 nm, followed by another dip at 745 nm, as the number of plasmonic chains diminishes because they are being welded into strings. Correspondingly, the strings' characteristic resonance appears at 1100 nm. The theoretical simulation data are in very good agreement with the experimental results and demonstrate that the breadth of the plasmon resonance around 1100 nm is due to a distribution of welding bridge thickness (or thread width). The authors also demonstrated that the nanowelding is caused by nonthermal ablation. Keeping the same average optical power, they repeated the experiment with two different laser sources: a CW laser and an ultrafast laser with lower peak power. Neither of these two control experiments resulted in nanowelding.

Figure 3c-iii displays another example of nanoparticle joining by pulsed laser light.[200] In this case, gold nanorods ($\approx$42 nm by $\approx$15 nm) were used and they were assembled into strings using two different surface molecules. Only one of these molecules was a linker and it attached preferentially to the ends of the nanorods. As a result, the nanorods formed elongated chains, as shown in Figure 3c-iv. The chains had a plasmon resonance at 960 nm and they were subsequently illuminated at 1030 nm with an ultrafast laser (100 fs, 1 kHz, fluence 0.85 mJ cm^{-2}). The resulting welding is demonstrated by the transmission electron microscopy (TEM) images in Figure 3c-v.

4. Heating up the Environment

In Figure 1, following energy transfer from light to the electrons, and from the electrons to the lattice, the lattice transfers energy to the environment in the form of heat. The heat transfer occurs typically at the nanosecond timescale. The temperature $T(\mathbf{r}, t)$ at position $\mathbf{r}$ outside the nanoparticle and at time t can be described based on the heat transfer model developed by Goldenberg and Tranter.[201] The model considers a homogeneous, spherical nanoparticle that is uniformly heated within an infinite homogeneous medium and it provides a useful intuitive understanding.[202] It proceeds from the same heat transfer equation as in Equation (4) and (5)[203]

$$\rho(\mathbf{r})c(\mathbf{r})\frac{\partial T(\mathbf{r},t)}{\partial t} = K\Delta T(\mathbf{r},t) + S(\mathbf{r},t) \tag{6}$$

where $\rho(\mathbf{r})$ is the mass density, $c(\mathbf{r})$ is the specific heat, K ($K_{Au}^{@20\,°C} = 310$ W m^{-1} K^{-1} and $K_{Ag}^{@20\,°C} = 406$ W m^{-1} K^{-1}) is the thermal conductivity (assumed constant for simplicity) and $S(\mathbf{r}, t)$ is a source term. The source term arises from the heat generation inside the nanoparticle, due to light. It can be

written as $S = \sigma_{abs}\, I$ where σ_{abs} is the absorption cross section of the nanoparticle and I is the intensity of light.[204] The source term can further be expressed as a function of a time dependent electric field $\mathbf{E}(\mathbf{r}, t)$ according to[205]

$$S(\mathbf{r}) = \frac{\omega}{2\pi}Im[\varepsilon(\mathbf{r},\omega)]|\mathbf{E}(\mathbf{r},t)|^2 \tag{7}$$

where ε is the electric permittivity of the nanoparticle material and ω is the frequency of light.

In the steady state, for continuous-wave illumination, or for pulsed light illumination with very high repetition rate, compared to the heat transfer rates in the system, a simplified time-independent heat equation can be written: $K\Delta T(\mathbf{r}) = -S(\mathbf{r})$. Then, for a single spherical nanoparticle, taking ΔT as the temperature difference with the ambient temperature[206]

$$\Delta T(\mathbf{r}) = \frac{V_{NP}S}{4\pi Kr} \tag{8}$$

where V_{NP} is the volume of the nanoparticle.

At the surface plasmon resonance, there is a peak in σ_{abs} that translates into a peak in temperature increase.[206] It should be noted that this intuitive model does not take into account the possible formation of a vapor bubble around the nanoparticle.[65]

The environmental heating opens up a plethora of useful applications. This section reviews a selection of the most tantalizing future advancements. First, we review the emerging field of nanorobotics, where scientists endeavor to create materials and machines, which can controllably transfer energy at the nanoscale with the help of thermoplasmonics. We then delve into the world of photothermal cancer therapy. With their low toxicity, tuneable optical properties, and ease of functionalization, Au NPs offer an enticing approach to targeting cancer cells. Once accumulated around a cancer cell, the Au NP can be illuminated (with typically near-IR light) either from outside the body to target for example skin or breast cancers, or via an endoscopic procedure with an optical fiber to address other cancers that are located deeper in the human body (such as lung cancer). The third emerging application we review is photothermal steam generation. In photothermal steam generation, plasmonic NPs are used for their quick conversion of solar into thermal energy. The fast speed of this energy conversion results in the production of vapor bubbles that surround the NPs without heating up the rest of the surrounding liquid. Photothermal steam generation has applications in clean water production, sterilization of medical instruments, and in concentrating solar power systems. The last application of environmental heating that we review in this section is heat-assisted magnetic recording. By using plasmonic NPs' key ability to concentrate light into hotspots, this application holds great promise in delivering the next level of technology to achieve unprecedented magnetic data storage densities.

4.1. Nanorobotics

Thermoplasmonics is an emerging hot topic that offers a route to controllable actuation at the nanoscale[47,48] and reversible plasmon tuning of sensing devices.[49,51] The ability to manipulate
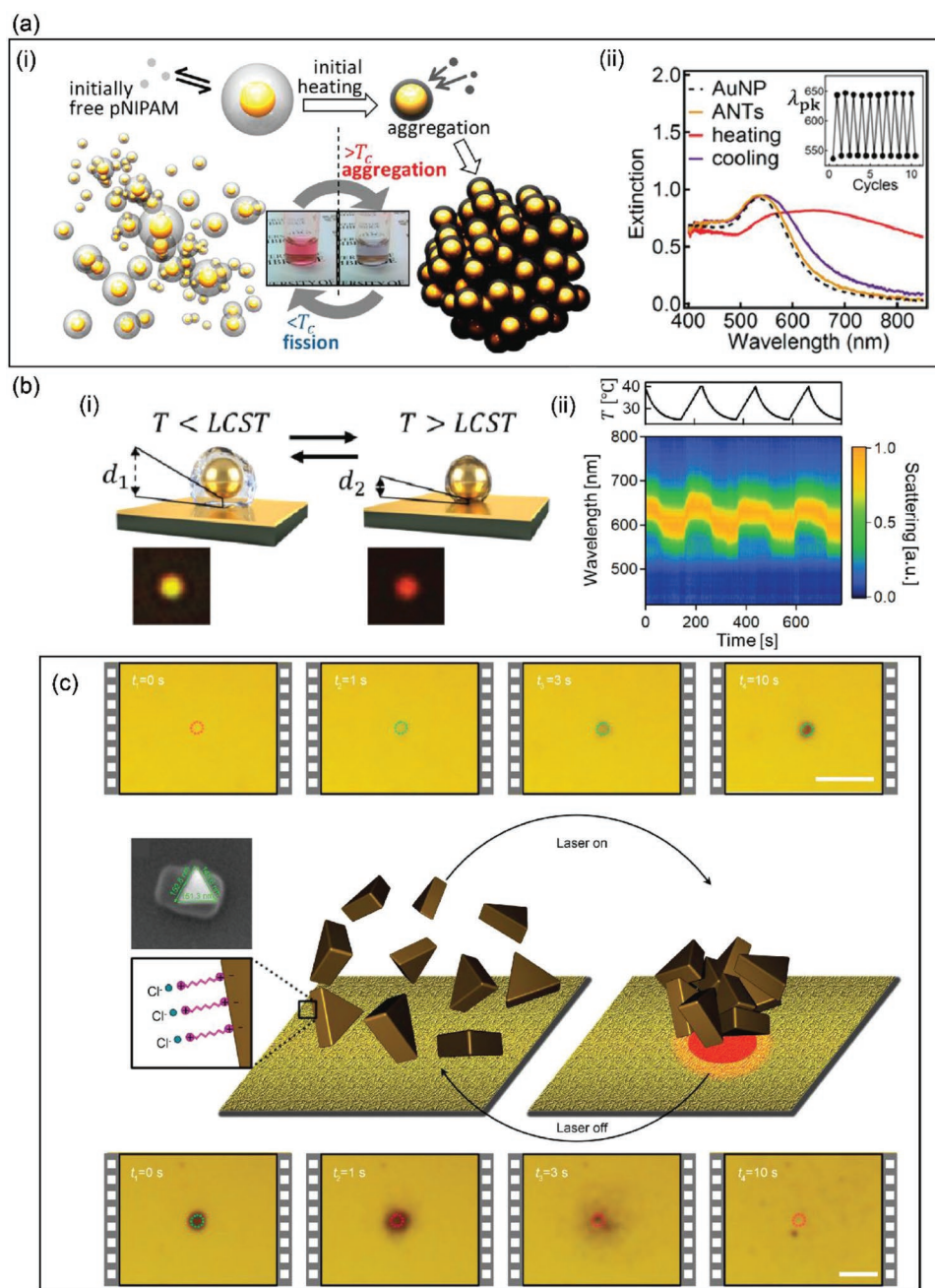
Figure 4. Plasmonic nanorobotics: optical sculpting at the nanoscale. a-i) Reversible assembly of actuating nanotransducers (ANTs). Formation of pNIPAM-coated Au nanoparticles by mixing in solution, and heating above T_c = 32 °C to attach pNIPAM onto Au. In deflated state, NPs aggregate tightly together (blue sol). Cooling then explosively splits clusters into individual ANTs (red sol). Further heating and cooling result in reversible fission and aggregation. a-ii) Extinction spectra of Au NPs initially (black) and in 40×10^{-6} M pNIPAM (orange), under laser heating (red) and cooled (purple). Reproduced with permission.[48] Copyright 2016, The author(s). Published by National Academy of Sciences. b-i) Controllable and reversible oscillation of the ANTs up and down on a Au mirror by thermoplasmonic heating. b-ii) Optically monitoring the reversible switching of plasmons through many cycles of heating and cooling. Reproduced with permission.[49] Copyright 2018, Wiley-VCH. c) Light-directed reversible assembly of plasmonic nanoparticles based on plasmon-enhanced thermophoresis. Schematic representation of the light-directed reversible assembly of positively charged AuNTs functionalized with cetyltrimethylammonium chloride (CTAC). Inset: scanning electron microscopy image of a single AuNT on the Au nanoisland substrate. Top: successive optical images during light-directed assembly of AuNTs. Bottom: successive optical images showing the disassembly of an AuNT aggregate after the laser is turned off. The red and blue dotted circles indicate that the laser is off and on, respectively. Scale bars: 10 μm. Reproduced with permission.[213] Copyright 2018, American Chemical Society.

nanoparticles in order to create and steer nanostructures is essential in many applications such as drug delivery,[207] noninvasive microsurgery,[208,209] nanoassembly, and fabrication.[50,51]

Figure 4 shows some examples of using thermoplasmonics in the exciting new field of nanorobotics. Ding et al. demonstrated the assembly of light-induced actuating nanotransducers

(ANTs), see Figure 4a-i,ii.[48] Such actuators allow the transformation of thermal energy into physical motion, essential to applications in robotics,[208] sensing,[210] storage devices, and smart windows.[211] By binding the temperature-responsive polymer pNIPAM to charged spherical Au nanoparticles, the authors were able to control the formation of Au clusters under light illumination. These clusters are capable of storing large amounts of elastic energy (1000 $k_B T$ per cycle), which can be rapidly (>MHz) released with a control light pulse. To achieve such fast actuation, the authors make use of the properties of the pNIPAM polymer, which is hydrophilic below a critical temperature ($T_c = 32$ °C), and highly hydrophobic above it. Therefore, by addressing the plasmon resonance of the pNIPAM coated Au NPs (shown in Figure 4a) with a 532 nm green CW laser, the polymer can be locally heated to above T_c. This heating causes water to be expelled from the polymer, thereby leading to aggregation of neighboring Au NPs in the citrate-stabilized solution. Since the hydrophobicity of pNIPAM is reversible, upon the end of the light pulse, the Au NPs are explosively repelled from each other. The elastic force exerted on the NPs is reported to be on the order of 5 nN, i.e., three orders of magnitude larger than what is attainable by current molecular motors and artificial muscles.[212] Recently, Turek and colleagues demonstrated an application of pNIPAM for creating DNA origami flexors.[50] Typically, a DNA origami consists of a long biological chain, referred to as the scaffold, with many short synthetic staples. In this study, the authors used a plate-like DNA origami, with a flexible hinge in the middle. They introduced pNIPAM-modified staples on either side of the flexible region. An Au NP on one plate and a fluorescent molecule (Cy5) on the other plate were used to monitor the flexor behavior in real time. By heating up the system above the critical temperature of pNIPAM, this construction caused the DNA origami to close. The authors were able to track the DNA origami behavior in real time by observing the light emission from the Cy5 molecule. Enhanced fluorescence from the Cy5 molecule was only observed in the closed state of the DNA origami, when the Cy5 molecule was in contact with the Au NP.[50]

Until recently, a fundamental issue underlying the wider use of pNIPAM based plasmonic actuators was the lack of more detailed understanding of the way that pNIPAM interacts with Au NPs. Such understanding is crucial for achieving reproducible and tunable plasmonic resonance shifts. Indeed, in some cases the hydrophobic contraction of pNIPAM, when heated to above its critical temperature, has failed to cause a shift in the plasmonic resonance of the Au NPs. This failure is due to electrostatic repulsion between the Au NPs. By using different ligand terminations of pNIPAM, Turek et al. were able to study the charge repulsion effect between the Au NPs in more detail.[52] A direct comparison between -SH, -COOH, -H, and -NH₂ terminated pNIPAM coatings showed that the biggest redshift of the plasmon and largest NP aggregates were achieved with pNIPAM-NH₂. This result is in contradiction with the hypothesis that the most effective actuation should be achieved with pNIPAM-SH, which forms the strongest bond with Au (out of all investigated terminations). The authors explain the difference in performance between pNIPAM of different terminations by considering the role of the surface charge of the Au NPs. They concluded that in the case of amine-terminated pNIPAM, the charge of any residual citrate groups, which remain trapped after the Au NPs have been functionalized, is screened by the amine groups. Therefore, the electrostatic repulsion between the Au NPs is minimized and the measured plasmonic shift is the strongest.[52]

Further, by exploiting the capability of forming large aggregates of Au NPs with pNIPAM coating, Cormier and colleagues demonstrated that it is possible to form self-assembled plasmonic metafilms that can be triggered to change color when illuminated with light.[53] They demonstrated the formation of such metafilms on a silicon substrate and proposed an application in water pumping.[53] In a different study shown in Figure 4b-i,ii, Cormier et al. placed pNIPAM-coated Au NPs on a Au substrate to create an optically controlled nano-oscillator.[49] Due to the thermal contraction and expansion of the pNIPAM coating when the Au NP was heated up with green light, the NP was observed to oscillate above the Au substrate. The authors were able to track the NP oscillations in real time by observing the spectral shift of the plasmonic resonance due to the change in the nanocavity width between the Au NP and the bulk Au substrate.[49] In addition, in a similar experimental setup Ding et al. demonstrated that the plasmon resonance of Au NPs could be controllably tuned by triggering a polymerization reaction within the gap between the NP and the Au substrate.[51] In this experiment, the Au substrate was coated with a self-assembled monolayer of thiophenol and Au NPs were then drop-cast on top. By immersing the NPs in a bulk monomer of divinylbenzene (DVB) and illuminating them with 635 nm CW laser, a polymerization reaction was triggered in the gap between the NP and the Au substrate. This polymerization led to blue shifting the plasmon resonance of the Au NP by about 70 nm. A similar effect was also observed for NIPAM polymerization. The proposed mechanism to explain the in situ polymerization reaction within the nanocavity between the Au NP and the substrate is based on plasmon generated hot electrons and was demonstrated to be self-limiting.[51] Such tunable plasmonic hot spots are exciting candidates for studying localized hot electron photochemical reactions and for plasmon-tuned sensing devices. One example of using such "NP-on-mirror" geometry for actuation was demonstrated by Kos et al.[40] In this experiment, the authors fabricated devices where an Al₂O₃ film was sandwiched between an Au substrate and a sheet of single layer graphene (SLG). Au NPs were deposited underneath the SLG for optical tracking. Applying a bias voltage to the Au substrate caused a reversible redox reaction, converting the Al₂O₃ film into O₂ bubbles and metallic Al. The O₂ bubbles were trapped underneath the graphene sheet, causing it to deform and actuate. The sensitivity of the plasmonic resonance of the Au NPs to the size of the nanocavity between the Au substrate and the Au NP allowed the authors to track bubble formation in real time. Similar to the previous examples, the O₂ bubbles caused a strong blueshift of the Au NP plasmon resonance.[40]

Thermoplasmonics can also be used to fabricate tightly packed nanostructures with tunable structural, optical and electrical properties. An example of such an experiment is shown in Figure 4c. In the work by Lin et al. Au nanotriangles (AuNTs) were suspended in an aqueous solution of cetiltrimethylammonium chloride (CTAC).[213] CTAC is nonphotoresponsive and it forms a positively charged hydrophilic layer on the surface of

**ADVANCED
SCIENCE NEWS**
www.advancedsciencenews.com

**ADVANCED
OPTICAL
MATERIALS**
www.advopticalmat.de

the AuNTs, which is surrounded by Cl^- ions. The thus formed bilayer around the AuNTs has thermophoresic properties that can be utilized by introducing a plasmonic surface underneath the AuNT dispersion. The authors used a substrate of Au nanoislands. Upon illumination with a 532 nm laser beam, the nanoislands undergo plasmonic heating, leading to a local temperature gradient in the surrounding solution. This temperature gradient induces a local electric field, which in turn causes the AuNTs to migrate and assemble at the laser spot. This process is schematically illustrated in Figure 4c. The top and the bottom panels of the figure show optical images of the reversible assembly and disassembly of such a nanostructure. The authors further demonstrate that the thus assembled Au nanostructures can be sculpted into different patterns and used for measuring the in situ surface enhanced Raman scattering (SERS) response of different molecules.

It is important to note that by contrast to standard nanotweezing schemes, all examples in Figure 4 use much lower laser powers (a few mW or less) to manipulate and assemble nanostructures. In this context, recently Lin et al. showed that thermophoresis can also be used to sculpt structures into versatile shapes by selectively manipulating individual particles of different material compositions, sizes and shapes.[214]

Another interesting example of thermoplasmonic nanoactuation is the use of a Au NP in a light-controlled nanovalve for on-command drug release.[207] In this experiment, Croissant and Zink used Au on mesoporous silica core–shell nanoparticles and preloaded them with cargo molecules. Upon illumination of the NPs with a CW diode laser tuned to the plasmon frequency of the Au core, the silica pores opened and released the cargo molecules.

4.2. Cancer Treatment

Plasmonic NPs can act as effective nanoheaters, upon excitation at the resonant frequency. This property can serve in cancer treatment to selectively heat tumor cells. The resulting treatment is known as photothermal therapy (PTT). In the past few years, it has been the subject of intensive scientific research.[215]

A schematic illustration of PTT is provided in **Figure 5**a. Plasmonic nanoparticles (surface-coated in the illustration) are injected either directly into the tumor site or intravenously and gather in the tumor due to mechanisms further discussed below. Subsequently, the tumor is irradiated by laser light with a wavelength matching a plasmonic resonance, which causes the nanoparticles to heat up and increase the temperature of their surroundings. Sufficient increase of the temperature of tissues leads to cell death through hyperthermia, which triggers apoptosis (death based on a genetic mechanism)[216] or causes necrosis directly.[217–219]

In order to prevent damage to healthy cells, it is desirable for the NPs to exclusively gather in the tumor. Some form of NP targeting is therefore essential. Passive targeting appears in the body naturally due to the enhanced permeability and retention (EPR) effect.[57,220] The EPR effect is caused by the biological differences between the cancerous and healthy tissues. The increased leakiness of the blood vessels in the tumor site allows for NPs between 6 nm and 2 μm in size to easily transfer from the blood to the tumor (enhanced permeability). Moreover, there is a diminished drainage of the cancerous tissue by lymphatic vessels, which leads to enhanced retention.[57]

Active targeting has been explored as a way to further increase the proportion of the injected NPs that gather at the tumor sites. This method consists of coating the surface of the NPs with molecules that bind to specific markers, overexpressed in the targeted type of cancer.[221–223] Molecules, such as transferrin or single-chain variable fragment peptide, have been used to coat (functionalize) Au NPs.[224,225] However, the improvement of the accumulation of NPs in tumors due to active targeting has been limited so far.[64] While the effects on the NP distribution in the body have been small, it has been shown that the targeting agents can affect whether the NPs accumulate inside or outside of the cells.[224–226]

Important properties of Au NPs, such as their cell uptake and biodistribution, are affected by the design of the NPs.[227] Modification of the shape and size of the NPs also provides a way to tailor the LSPR frequency to the first or second biological transparency windows (650–950 and 1000–1350 nm, respectively).[228] Deeper penetration of light into the tissues is achieved in these windows.

Mostly NPs made of Au have been studied for use in PTT, due to their chemical inertness and the easiness of the functionalization of their surface.[56] Au NPs of various shapes have been prepared. These include nanoshells,[229] nanorods,[230] nanostars,[231] nanocages,[232] nanomatryoshkas,[233] and more.[227,234–236]

PTT has been tested both in vitro and in vivo in animal models.[58–60,229,237,238] Figure 5b shows results of photothermal treatment of mice with human prostate cancer performed by Stern et al.[237] The authors injected polyethylene glycol (PEG) coated Au nanoshells with 110 nm SiO_2 core and 10 nm Au shell into tail veins of the mice. In order to leave enough time for the NPs to accumulate in the tumor, laser treatment (laser wavelength = 810 nm, fluence = 4 W cm^{-2}) was commenced 18 h later. The left image in Figure 5b shows a photo of a mouse from the control group. A complete disappearance of the tumor is observed for the mouse in the group treated with PTT (right image in Figure 5b).

Photographs of a dog suffering from a natural mammary tumor are shown in the left and middle images of Figure 5c. The dog was administered with a dose of Au nanorods (50 nm long, 12 nm wide) which were injected directly into the tumor. The tumor site was subsequently irradiated with pulsed laser light of wavelength of 808 nm and peak power density of 2 W cm^{-2}. The image on the right of Figure 5c shows the abdomen of the dog after treatment. The abdomen did not show any sign of cancer.[238]

Figure 5d shows photographs of a cat from a case study performed by Abdoon et al.[60] In the image on the left, a mammary gland tumor is visible. Two sessions of PTT with Au nanorods injected intratumorally were performed two weeks apart. Illumination was performed with a CW laser, at 808 nm, with a power of 50 mW cm^{-2}. A complete disappearance of the tumor was observed, as shown in the image on the right. The treatment had no effect on the fertility of the cat and it was able to use the formerly affected nipple to feed its kittens (bottom of Figure 5d).

**ADVANCED
SCIENCE NEWS**

www.advancedsciencenews.com

**ADVANCED
OPTICAL
MATERIALS**

www.advopticalmat.de

Figure 5. Plasmonic nanoparticles successfully used for cancer treatment in several animal models. a) The principle of photothermal therapy. Au nanoparticles (coated with liposomes in this case) are injected in the body and gather in the tumor. Upon irradiation, these nanoparticles produce heat, which destroys the tumor. Reproduced with permission.[243] Copyright 2015, the American Chemical Society. b) A photo of a mouse with human prostate cancer is shown on the left. The image on the right shows a complete disappearance of a tumor after treatment with photothermal therapy. Reproduced with permission.[237] Copyright 2008, Elsevier. c) A photo of the abdomen of a dog with a natural mammary tumor before (left and center) and after being treated with photothermal therapy (right). Reproduced with permission.[238] Copyright 2016, Elsevier. d) A cat with a mammary gland tumor before (top left) and after (top right) photothermal therapy. The cat could feed her kittens with the affected nipple after the treatment (bottom). Adapted under the terms of the Creative Commons Attributions License.[60] Copyright 2015, The Author(s). Published by Longdom Publishing.

Several clinical trials have been conducted on humans using Au nanoshells with SiO_2 core and Au shell. These trials concentrated on the adverse effects of the Au nanoparticles and the success rate of the treatment. In the very first clinical trial, Au nanoshells were used to treat tumors in the head and neck.[61] The results published online indicate that 4 out of 11 people did experience adverse effects after being treated with Au nanoparticles. The efficacy of the treatment has not been reported. The second trial aimed at treatment of metastatic lung tumors.[62] However, it only had one participant and ended prematurely. The third trial is still ongoing.[63]

Au NPs can be used as carriers to provide targeted release of anticancer drugs in tumors.[239,240] While chemotherapy is an effective cancer treatment, it presents many adverse effects. Au NPs, such as mesoporous silica-encapsulated Au nanorods or Au nanocages, can be used to deliver chemotherapeutic drugs to a tumor where the drug is released upon irradiation with NIR light.[241,242] This combination therapy has the advantage of minimizing adverse effects as the chemotherapeutic drugs are released in the tumor site only. Furthermore, it has been shown that the combination therapy is more effective than PTT or chemotherapy alone.[241]

PTT is a very promising and minimally invasive method of treating cancer using plasmonic NPs. Future use in cancer treatment depends on the results of clinical trials and more research into toxicity of Au nanoparticles. Targeting also remains an issue as usually less than 10% of intravenously injected Au nanoparticles gather in the tumor.[64,223] Reproducibility and comparability of different studies have also been identified as problematic for identifying the most efficient NP design.[64] Finally, the high cost of PTT treatment may also slow down clinical translation in the future.[64]

4.3. Steam Generation

When NPs are dispersed in a medium, such as water or ice, the heat emitted to their surroundings upon irradiation can increase the temperature of the medium enough for the medium to undergo a phase change.[65,244] Numerous applications of this phenomenon have been proposed, especially for the case when solar illumination is used as the energy source. Such applications include desalination and sterilization of medical instruments in areas with limited resources. Uses in clean electricity production have also been suggested. Compared to current solar receivers, when NP solutions are used, light absorption appears throughout the whole volume of the working liquid compared to absorption only on a surface. Moreover with NPs, the surface temperature of the systems is lower than in the case of conventional systems resulting in lower losses to the surroundings and thus higher efficiency.[245]

The first demonstration of using plasmonic NPs for producing steam/vapor was performed by Neumann et al.[65] The authors used SiO_2/Au nanoshells dispersed in water in a container. The container was placed in an ice bath. Within 5 s of illumination with focused sunlight, while the temperature of the water was still below the boiling point, steam generation was observed. The authors estimated that 80% of absorbed energy was used to create steam while the remaining energy was dissipated into the bulk of the liquid.

The exact mechanism behind steam generation has been a subject of discussion. Neumann et al. suggested that upon irradiation a small bubble is created around a NP.[65] The bubble thermally insulates the NP from the bulk fluid and hence limits heating of the liquid as a whole. As the bubble grows, the effective density of the NP-bubble complex becomes lower than the density of water which results in buoyancy force moving the NP toward the surface of the liquid. Once the NP reaches the surface, the bubble bursts and steam is released. Hogan et al. showed that both the absorption and the scattering by the NPs (as illustrated in **Figure 6**a) are important in the process of steam production.[246] By comparing numerical simulations with experiments the authors demonstrated that, depending on the concentration of the NPs, the light can be trapped in a small volume of the liquid near the surface causing highly localized heating. In the work of Ni et al., the authors investigated steam generation in solutions of graphitized carbon black, carbon black and graphene in water.[245] Their results indicated that the heating of the bulk fluid was the main mechanism behind the observed steam generation as compared to nanobubble formation.

Some of the potential wide-ranging applications of solar steam production have already been demonstrated with proof-of-concept devices. Neumann et al. built a solar autoclave for sterilization of medical instruments.[247] A Fresnel lens was used to focus solar light into a water container with a solution of Au nanoshells with a concentration of 10^{10} nanoshells per m^3. The system could maintain a temperature of 132 °C for 5 min, which was sufficient for successful sterilization.

Irradiation by focused solar light has also been shown to enable distillation of ethanol when plasmonic NPs were used.[65] Interestingly, higher concentrations of ethanol were achieved than with standard flash distillation. Importantly, no NPs were detected in the product, which shows that no NPs escape the liquid medium during evaporation. Recently, it was demonstrated that a similar method could be used for production of cellulosic bioethanol from sugar cane or coastal hay using only solar energy as the energy source.[248]

In order to maximize the efficiency of solar steam production, various designs of plasmonic absorbers have been suggested. As already mentioned, Neumann et al. used SiO_2 core/Au shell NPs in their experiments.[65] Zielinski et al. made hollow mesoporous Au/Ag alloy nanoshells by nanomasking followed by partial galvanic replacement.[249] These nanoshells are schematically shown in Figure 6b. In such NPs steam is generated both on the inside and the outside of the NPs. The steam production rates are higher compared to Au nanoshells with a solid core and the NPs feature the added benefit of greater buoyancy and thus lower sedimentation rates.

Plasmonic absorbers consisting of mesoporous films with built-in NPs that float on the surface of water present another approach to steam production. The floating design focuses the heating power to a very thin layer on the water-air interface and thus reduces the losses due to bulk heating. At the same time, water is constantly in contact with the plasmonic nanoheaters due to the porous structure of the membranes.

Figure 6c shows an illustration of a floating plasmonic absorber fabricated by Chen et al.[250] In the device, Au NPs are
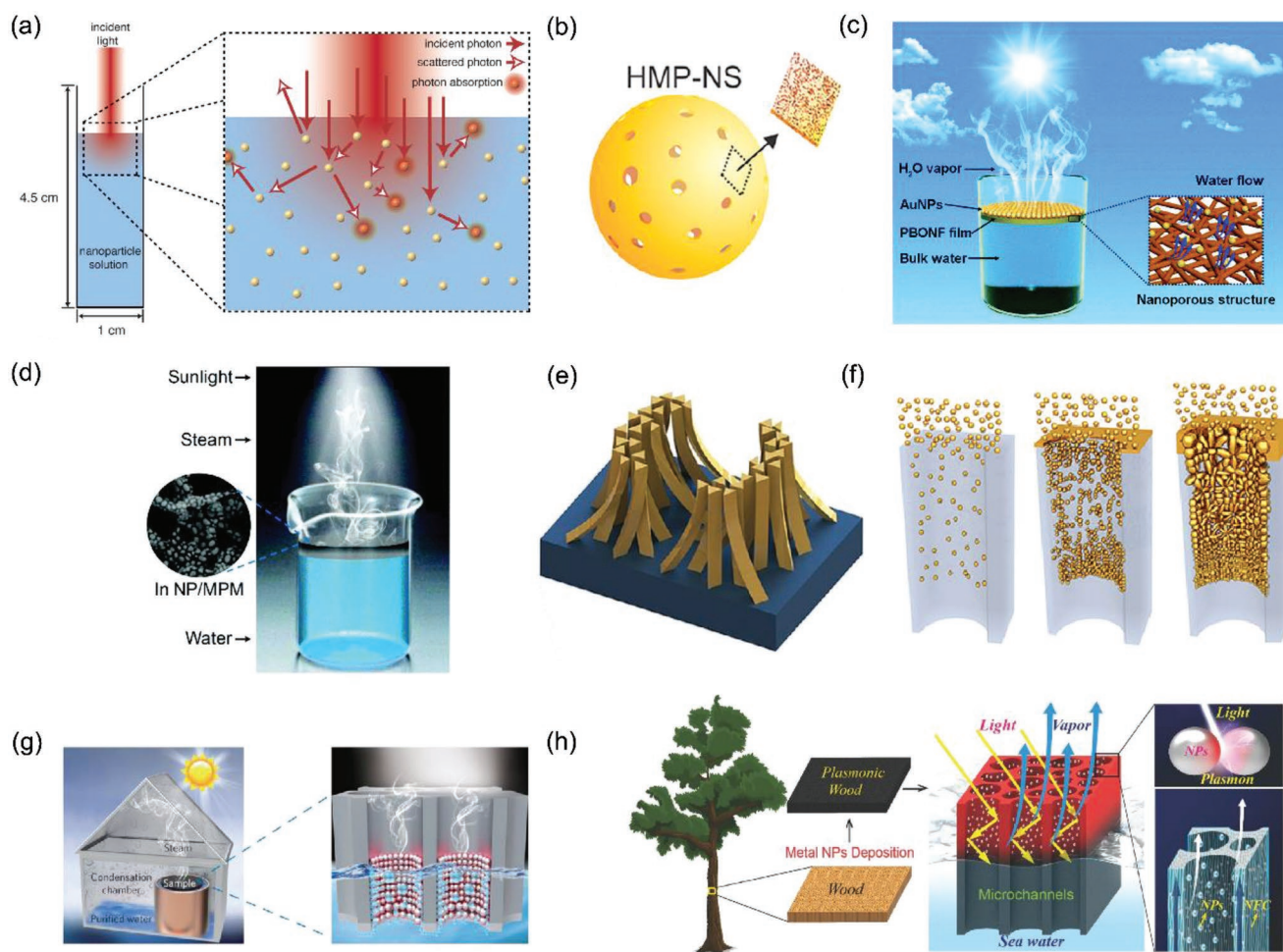
Figure 6. Steam generation using plasmonic absorbers. a) An illustration of the principle of steam generation using Au nanoparticles dispersed in water. Adapted with permission.[246] Copyright 2014, the American Chemical Society. b) Hollow mesoporous plasmonic nanoshells (HMP-NS) can be used to generate steam. These particles have the advantage of lower sedimentation rates than Au nanospheres with a solid core. Adapted with permission.[249] Copyright 2016, the American Chemical Society. c) Au nanoparticles can be built into a poly(p-phenylene benzobisoxazole) nanofiber (PBONF) film which floats on the surface of water. Reproduced with permission.[250] Copyright 2018, the Royal Society of Chemistry. d) Plasmonic In nanoparticles in a microporous membrane (MPM) can be used for steam generation. Reproduced with permission.[251] Copyright 2017, the Royal Society of Chemistry. e) A membrane made of self-aggregated nanowires coated with Au can be used as a plasmonic absorber. Adapted under the terms of the Creative Commons Attribution 4.0 License.[252] Copyright 2015, The Author(s). Published by Springer Nature. f) Self-assembly of Au nanoparticles in a porous Al$_2$O$_3$ substrate creates an almost ideal plasmonic absorber. Adapted with permission.[253] Copyright 2016, The Authors, some rights reserved; exclusive licensee American Association for the Advancement of Science. Distributed under a Creative Commons Attribution NonCommercial License 4.0 (CC BY-NC), http://creativecommons.org/licenses/by-nc/4.0/. g) Self-assembly of Al nanoparticles in a porous substrate. Reproduced with permission.[254] Copyright 2016, Springer Nature. h) Natural wood contains microchannels and can be used as a nanoporous template for self-assembly of gold nanoparticles. Reproduced with permission.[255] Copyright 2017, Wiley-VCH.

supported by a nanoporous film consisting of poly(p-phenylene benzobisoxazole) nanofibers (PBONFs). The PBONF film is extremely durable and the authors suggest that their device could be used for clean water production in extreme environments including space.

Zhang et al. explored In NPs as a cheaper alternative to Au NPs for use as plasmonic absorbers.[251] Indium was thermally evaporated on a microporous membrane (MPM) and the device was then used for steam production when floating on water as shown in Figure 6d. The deposition of In led to creation of NPs that started merging and forming clusters as the deposition time was increased. The resulting NPs thus had varying

shapes and sizes, which affected the wavelength and width of the plasmon resonance and led to the NPs absorbing in a wide range of wavelengths. The authors stressed the benefit of easy fabrication of the In NP covered membranes and the calculated large heating efficiency of In NPs.

High absorption and spectral overlap with sunlight are essential for achieving efficient solar steam production. A wide wavelength range absorber was created by Bae et al.[252] This absorber was made of self-aggregated nanowires coated with Au and is shown in Figure 3e. An average absorption of 91% over the range from 400 nm to 2500 nm and steam generation with an efficiency of 57% was reported.

Zhou et al. manufactured a plasmonic absorber made of Au NPs of various sizes, which self-assembled in a porous Al_2O_3 substrate (Figure 6f).[253] The authors reported an absorbance of ≈99% in the wide wavelength range from 400 nm to 10 µm. Steam generation efficiency of more than 90% was reported.

Another example of a self-assembled plasmonic absorber is shown in Figure 6g. The absorber is made of Al NPs. While the LSPR in Al NPs usually lies in the UV region, the authors made use of the red-shift, due to plasmon hybridization in the closely spaced Al NPs. The absorption of longer wavelengths is further enhanced due to a thin oxide layer, which develops on the surface of the NPs and influences the effective permittivity of the NP surroundings. The authors reported that the self-assembled structures absorbed more than 96% of the solar spectrum and exhibited high energy transfer efficiency.[254] Furthermore, they were made of cheap and abundant materials.

Zhu et al. also studied NPs in a nanoporous substrate, but in their case natural wood was used as the substrate (Figure 6h).[255] Wood already has pores that are used, for instance, to transport water in a tree. Similarly, when plasmonic nanoparticles (Pd, Au and Ag in this case) are deposited on the walls of the pores, water is transported to them, heated up, and eventually evaporated. The authors claimed that their samples absorbed ≈99% of light with wavelengths between 200 and 2500 nm. They also demonstrated efficient (85%) steam production when irradiated with focused light (10 kW m^{-2}).

4.4. Heat-Assisted Magnetic Recording

The unique ability of plasmonic materials to focus electromagnetic fields into hotspots has wide-ranging potential applications, including enabling magnetic data storage with much higher storage densities than currently available.

A large proportion of electronic data is stored in hard disk drives (HDDs) that offer lower cost per stored unit of information than available alternatives. However, the storage densities achievable with the current technology are limited to ≈1 Tb in.$^{-2}$.[256] Heat-assisted magnetic recording (HAMR) has been proposed as a solution to the problem.

HDDs consist of a magnetic recording medium rotating at high speed and a write/read head that is located only a few nm above the surface of the recording medium. The recording medium itself is made of a polycrystalline magnetic material, where the data is stored in individual magnetic domains with different magnetization orientation. In order to increase the storage density of HDDs, the size of the magnetic domains (that act as individual bits) has to be decreased. However, decrease in the size of the domains also reduces their anisotropy energy and thus makes them more susceptible to thermal excitations that can flip the direction of their magnetization, thereby scrambling the stored information.

Materials with high coercivities can sustain smaller magnetic domains due to their larger magnetic anisotropy. However, these coercivities become too high to overcome upon recording information by the currently available write heads. In HAMR, the temperature of the recording medium is temporarily increased above its Curie temperature in order to write

information. Plasmonic materials are useful in this process due to their ability to focus electromagnetic fields into small volumes, which allows for heating the recording medium locally with high spatial resolution.[257] The feasibility of HAMR with plasmonic near-field transducers (NFTs) integrated in the write head has been demonstrated for example by Challener et al. and Stipe et al.[258,259]

5. Conclusion

This review presented some of the phenomena that arise upon exciting surface plasmon resonances in metallic nanoparticles.

We began by highlighting the processes of radiative decay in plasmonic nanoparticles (Section 2.1). Nonlinear optical processes are among the fastest such processes and they greatly benefit from the electromagnetic enhancements in plasmonic "hot spots." We highlighted four directions where plasmonics plays an important role. First, plasmonic fields can be used to enhance the frequency conversion at the nanoscale, though it remains to be seen whether these enhancements will ever be able to replace current phase-matched materials. Second, plasmonic nanoparticles are serving as efficient labels for bioimaging, though there are number of alternative labels available, both organic and inorganic. Third, plasmonic nanoparticles find applications in developing nonlinear metasurfaces, though dielectric metasurfaces are growing more popular. Fourth, plasmonic near-field enhancements are revealing novel physical effects, solving decades old scientific problems; we can expect other such effects to be discovered in the future.

In the case of nonradiative decay, Landau damping leads to the creation of highly energetic (hot) electrons, in the conduction band of plasmonic nanoparticles. These hot electrons find applications in catalyzing chemical reactions and in splitting water molecules for fuel, as presented in Section 2.2.1. Even though plasmonic NPs offer a promising route to extending the spectral range of light used for photocalytic reactions from the UV to the visible and IR spectrum, the field of plasmon-assisted chemistry is still in its early years, with a number of big challenges ahead of it. The scaleability of production of NPs of selected sizes and shapes remains a challenge. Preserving the size, shape and purity of the plasmonic NPs is another formidable challenge that will need to be addressed before such catalysis can be scaled industrially. Moreover, our understanding of the effects of surface defects and impurities on the efficiency of plasmonically induced catalysis is at present very limited. Understanding the interplay between these hot electrons and the thermal effects could enable novel routes to controlling catalytic reactions.

Section 2.2.2 outlined how the properties of plasmonic NPs, including hot electron generation, can lead to an increase in the efficiency of solar cells and allow for new types of photodetectors. As the use of solar energy is becoming increasingly widespread there is a significant push toward increasing the efficiency of solar cells, e.g., through the integration of plasmonic NPs. Plasmonic NPs can increase the absorption of light due to scattering, hot electron generation and plasmon-induced resonance energy transfer. Key challenges ahead of the field are the integration of such plasmonic nanostructures into currently

**ADVANCED
SCIENCE NEWS**
www.advancedsciencenews.com

**ADVANCED
OPTICAL
MATERIALS**
www.advopticalmat.de

used solar cell materials, the reliable and cost-effective production of NPs of a desired size, shape and material composition, as well as the thorough understanding of the mechanisms that enhance the light-to-electricity conversion efficiency.

Section 3 discussed the effects related to the transfer of energy from hot electrons to the lattice. As shown in Section 3.1, the detection of phonons can serve to investigate the optical absorption in plasmonic NPs. Phonons also find useful applications in photoacoustic imaging.

In Section 3.2, we surveyed the three constitutive areas of nanometalworking, namely forming, cutting and joining. In each case, examples were presented, whereby the shape of nanostructures can be manipulated. Highly localized plasmonic hotspots are the tools of these manipulations, allowing ultrafast and targeted reshaping, at length scales much smaller than the wavelength of light. Nanometalworking with light is emerging as a promising route for assembling metamaterials, combining elements of both bottom-up and top-down nanofabrication.

Section 4 presented examples of plasmonic nanoparticles employed as nanoheaters. There are potential applications for this technology, which do not fall within the subsections we chose for this review. As an example, gold nanoparticles based coatings were recently prepared to control the alkali atom vapor pressure for quantum sensors.[260] This work constitutes an early exploration at the interface between plasmonics and atomic quantum optics. We can expect more such works to follow in this direction, as the potential gains for magnetometry, atomic traps, laser frequency stabilization, etc., are considerable.

Section 4.1. highlighted instances of light-controlled nanorobotics. ANTs constitute some of the most promising nano-actuators. They offer fast, controllable and powerful actuation forces. Moreover, they are flexible in size, shape and functionalization. They offer a route to remotely controlled and fully reversible bottom-up assembly of nanomachines, intelligent design of color changing windows, smart lighting and large-area photocromics for buildings, drug delivery through optically actuated nanovalves, enhanced catalysis and SERS detection, nanogenerators for powering nanomachines, artificial muscles and cartilages for soft nanorobotics, to name a few. Despite overcoming some key bottlenecks in the field of nanorobotics and showing great potential for future applications, these light-actuated thermoplasmonic systems still face a number of challenges, among which are the ability to controllably direct the actuation, the need for increased efficiency of the generated forces, and the routes for industrial level scalability.

Section 4.2 focused on using plasmonic nanoparticles in cancer treatment. Such treatments seem promising for certain types of cancer and they have progressed to the clinical trial stage. Plasmonic nanoparticles are also being investigated as drug carriers, which release their load at the desired location. Directing the NPs to the desired locations within the body remains an issue. Also, potential side effects need to be fully understood.

Section 4.3 presented the applications of plasmonic NPs in steam generation. Such applications range from sterilization of medical instruments to generation of renewable energy. We discussed two different approaches to steam generation in plasmonic systems: by dispersing the NPs within the volume of the liquid, or by floating plasmonic membranes on the surface of water. Each of these approaches has its advantages and disadvantages and is suitable for different applications. The fabrication of plasmonic NPs to be dispersed in the volume of a liquid is often relatively easy and scalable. These NPs act as volumetric heaters, which makes them suitable for applications in energy production. The floating systems generally have higher efficiencies and are useful for applications, such as desalination and drinking water production. The wider employment of such systems will depend on the cost of manufacturing the devices and the achievable lifetimes. It will also be interesting to see how the different designs perform in applications where high pressure steam is necessary.

The use of plasmonic nanostructures in heat-assisted magnetic recording systems was briefly discussed in Section 4.4. Heat-assisted magnetic recording allows denser magnetic storage but industrial integration of the progress seems slow, possibly due to the associated complexity costs.

Acknowledgements

Conflict of Interest

The authors declare no conflict of interest.

Keywords

[1] S. V. Boriskina, T. A. Cooper, L. Zeng, G. Ni, J. K. Tong, Y. Tsurimaki, Y. Huang, L. Meroueh, G. Mahan, G. Chen, *Adv. Opt. Photonics* **2017**, *9*, 775.

[2] C. Clavero, *Nat. Photonics* **2014**, *8*, 95.

[3] L. Ranno, S. D. Forno, J. Lischner, *npj Comput. Mater.* **2018**, *4*, 31.

[4] G. Baffou, R. Quidant, *Laser Photonics Rev.* **2013**, *7*, 171.

[5] F. Benz, R. Chikkaraddy, A. Salmon, H. Ohadi, B. de Nijs, J. Mertens, C. Carnegie, R. W. Bowman, J. J. Baumberg, *J. Phys. Chem. Lett.* **2016**, *7*, 2264.

[6] W.-S. Chang, B. Willingham, L. S. Slaughter, S. Dominguez-Medina, P. Swanglap, S. Link, *Acc. Chem. Res.* **2012**, *45*, 1936.

[7] S. Linic, P. Christopher, D. B. Ingram, *Nat. Mater.* **2011**, *10*, 911.

[8] K. Kneipp, Y. Wang, H. Kneipp, L. T. Perelman, I. Itzkan, R. R. Dasari, M. S. Feld, *Phys. Rev. Lett.* **1997**, *78*, 1667.

[9] S. Nie, *Science* **1997**, *275*, 1102.

[10] R. W. Boyd, *Nonlinear Optics*, Elsevier Academic Press Inc, San Diego, CA **2008**.

[11] N. C. Panoiu, W. E. I. Sha, D. Y. Lei, G.-C. Li, *J. Opt.* **2018**, *20*, 083001.

[12] P. A. Franken, A. E. Hill, C. W. Peters, G. Weinreich, *Phys. Rev. Lett.* **1961**, *7*, 118.

[13] N. Yu, F. Capasso, *Nat. Mater.* **2014**, *13*, 139.

[14] N. Yu, P. Genevet, M. A. Kats, F. Aieta, J.-P. Tetienne, F. Capasso, Z. Gaburro, *Science* **2011**, *334*, 333.

[15] G. Deka, C.-K. Sun, K. Fujita, S.-W. Chu, *Nanophotonics* **2017**, *6*, 31.

[16] W. Zheng, X. Liu, A. T. Hanbicki, B. T. Jonker, G. Lüpke, *Opt. Mater. Express* **2015**, *5*, 2597.

[17] M. Kauranen, A. V. Zayats, *Nat. Photonics* **2012**, *6*, 737.

[18] V. K. Valev, *Langmuir* **2012**, *28*, 15454.

[19] H. Harutyunyan, A. B. F. Martinson, D. Rosenmann, L. K. Khorashad, L. V. Besteiro, A. O. Govorov, G. P. Wiederrecht, *Nat. Nanotechnol.* **2015**, *10*, 770.

[20] S. Yu, Y. H. Kim, S. Y. Lee, H. D. Song, J. Yi, *Angew. Chem., Int. Ed.* **2014**, *53*, 11203.

[21] S. Mukherjee, F. Libisch, N. Large, O. Neumann, L. V. Brown, J. Cheng, J. B. Lassiter, E. A. Carter, P. Nordlander, N. J. Halas, *Nano Lett.* **2013**, *13*, 240.

[22] K. G. Reddy, T. G. Deepak, G. S. Anjusree, S. Thomas, S. Vadukumpully, K. R. V. Subramanian, S. V. Nair, A. S. Nair, *Phys. Chem. Chem. Phys.* **2014**, *16*, 6838.

[23] Z. Liu, W. Hou, P. Pavaskar, M. Aykol, S. B. Cronin, *Nano Lett.* **2011**, *11*, 1111.

[24] A. O. Govorov, H. Zhang, H. V. Demir, Y. K. Gun'ko, *Nano Today* **2014**, *9*, 85.

[25] X. Chen, Z. Zheng, X. Ke, E. Jaatinen, T. Xie, D. Wang, C. Guo, J. Zhao, H. Zhu, *Green Chem.* **2010**, *12*, 414.

[26] H. Zhu, X. Chen, Z. Zheng, X. Ke, E. Jaatinen, J. Zhao, C. Guo, T. Xie, D. Wang, *Chem. Commun.* **2009**, 7524.

[27] P. Mulvaney, *ACS Nano* **2015**, *9*, 2215.

[28] D. Bäuerle, *Laser Processing and Chemistry*, Springer, Berlin **2011**.

[29] A. Plech, P. Leiderer, J. Boneberg, *Laser Photonics Rev.* **2009**, *3*, 435.

[30] A. Plech, V. Kotaidis, M. Lorenc, J. Boneberg, *Nat. Phys.* **2006**, *2*, 44.

[31] Z. Wu, Y. Wu, W. He, X. Lin, J. Sun, Q. He, *Angew. Chem., Int. Ed.* **2013**, *52*, 7000.

[32] S. Sanchez, A. N. Ananth, V. M. Fomin, M. Viehrig, O. G. Schmidt, *J. Am. Chem. Soc.* **2011**, *133*, 14860.

[33] J. Katuri, X. Ma, M. M. Stanton, S. Sánchez, *Acc. Chem. Res.* **2017**, *50*, 2.

[34] D. Walker, M. Kübler, K. I. Morozov, P. Fischer, A. M. Leshansky, *Nano Lett.* **2015**, *15*, 4412.

[35] W. R. Browne, B. L. Feringa, *Nat. Nanotechnol.* **2006**, *1*, 25.

[36] M. Liu, T. Zentgraf, Y. Liu, G. Bartal, X. Zhang, *Nat. Nanotechnol.* **2010**, *5*, 570.

[37] S. K. Samanta, J. W. Bats, M. Schmittel, *Chem. Commun.* **2014**, *50*, 2364.

[38] L. Shao, Z.-J. Yang, D. Andrén, P. Johansson, M. Käll, *ACS Nano* **2015**, *9*, 12542.

[39] P. Ketterer, E. M. Willner, H. Dietz, *Sci. Adv.* **2016**, *2*, e1501209.

[40] D. Kos, H. P. A. G. Astier, G. Di Martino, J. Mertens, H. Ohadi, D. De Fazio, D. Yoon, Z. Zhao, A. Kuhn, A. C. Ferrari, C. J. B. Ford, J. J. Baumberg, *Small* **2018**, *14*, 1801599.

[41] Y. Ke, T. Meyer, W. M. Shih, G. Bellot, *Nat. Commun.* **2016**, *7*, 10935.

[42] S. Hernández-Ainsa, M. Ricci, L. Hilton, A. Aviñó, R. Eritja, U. F. Keyser, *Nano Lett.* **2016**, *16*, 4462.

[43] D. Liu, S. Balasubramanian, *Angew. Chem., Int. Ed.* **2003**, *42*, 5734.

[44] J. List, M. Weber, F. C. Simmel, *Angew. Chem., Int. Ed.* **2014**, *53*, 4236.

[45] S. Hernández-Ainsa, K. Misiunas, V. V. Thacker, E. A. Hemmig, U. F. Keyser, *Nano Lett.* **2014**, *14*, 1270.

[46] Y. Yang, M. Endo, K. Hidaka, H. Sugiyama, *J. Am. Chem. Soc.* **2012**, *134*, 20645.

[47] Q. Jiang, Q. Liu, Y. Shi, Z.-G. Wang, P. Zhan, J. Liu, C. Liu, H. Wang, X. Shi, L. Zhang, J. Sun, B. Ding, M. Liu, *Nano Lett.* **2017**, *17*, 7125.

[48] T. Ding, V. K. Valev, A. R. Salmon, C. J. Forman, S. K. Smoukov, O. A. Scherman, D. Frenkel, J. J. Baumberg, *Proc. Natl. Acad. Sci. USA* **2016**, *113*, 5503.

[49] S. Cormier, T. Ding, V. Turek, J. J. Baumberg, *Adv. Opt. Mater.* **2018**, *6*, 1701281.

[50] V. A. Turek, R. Chikkaraddy, S. Cormier, B. Stockham, T. Ding, U. F. Keyser, J. J. Baumberg, *Adv. Funct. Mater.* **2018**, *28*, 1706410.

[51] T. Ding, J. Mertens, A. Lombardi, O. A. Scherman, J. J. Baumberg, *ACS Photonics* **2017**, *4*, 1453.

[52] V. A. Turek, S. Cormier, B. Sierra-Martin, U. F. Keyser, T. Ding, J. J. Baumberg, *Adv. Opt. Mater.* **2018**, *6*, 1701270.

[53] S. Cormier, T. Ding, V. Turek, J. J. Baumberg, *Adv. Opt. Mater.* **2018**, *6*, 1800208.

[54] cytimmune, http://www.cytimmune.com/ (accessed: July 2019).

[55] nanospectra, https://www.nanospectra.com/ (accessed: July 2019).

[56] D. J. de Aberasturi, A. B. Serrano-Montes, L. M. Liz-Marzán, *Adv. Opt. Mater.* **2015**, *3*, 602.

[57] E. C. Dreaden, M. A. Mackey, X. Huang, B. Kang, M. A. El-Sayed, *Chem. Soc. Rev.* **2011**, *40*, 3391.

[58] G. von Maltzahn, J.-H. Park, A. Agrawal, N. K. Bandaru, S. K. Das, M. J. Sailor, S. N. Bhatia, *Cancer Res.* **2009**, *69*, 3892.

[59] M. R. K. Ali, I. M. Ibrahim, H. R. Ali, S. A. Selim, M. A. El-Sayed, *Int. J. Nanomed.* **2016**, *11*, 4849.

[60] A. Abdoon, E. Al-Ashkar, A. Shabaka, O. Kandil, W. Eisa, A. Shaban, H. Khaled, M. El Ashkar, M. El Shaer, A. Shaalan, M. El Sayed, *J. Nanomed. Nanotechnol.* **2015**, *6*, 1000324.

[61] Nanospectra Biosciences, Pilot Study of AuroLase(tm) Therapy in Refractory and/or Recurrent Tumors of the Head and Neck, http://clinicaltrials.gov/ct2/show/NCT00848042 (accessed: July 2019).

[62] Nanospectra Biosciences, Efficacy Study of AuroLase Therapy in Subjects With Primary and/or Metastatic Lung Tumors, http://clinicaltrials.gov/ct2/show/NCT01679470 (accessed: July 2019).

[63] Nanospectra Biosciences, MRI/US Fusion Imaging and Biopsy in Combination With Nanoparticle Directed Focal Therapy for Ablation of Prostate Tissue, https://clinicaltrials.gov/ct2/show/NCT02680535 (accessed: July 2019).

[64] N. S. Abadeer, C. J. Murphy, *J. Phys. Chem. C* **2016**, *120*, 4691.

[65] O. Neumann, A. S. Urban, J. Day, S. Lal, P. Nordlander, N. J. Halas, *ACS Nano* **2013**, *7*, 42.

[66] R. W. Boyd, *Nonlinear Optics*, Elsevier, Orlando **2003**.

[67] Y. R. Shen, *The Principles of Nonlinear Optics*, Wiley, New York **1984**.

[68] D. L. Mills, *Nonlinear Optics: Basic Concepts*, Springer, Berlin **1991**.

[69] N. Nookala, J. Lee, M. Tymchenko, J. Sebastian Gomez-Diaz, F. Demmerle, G. Boehm, K. Lai, G. Shvets, M.-C. Amann, A. Alu, M. Belkin, *Optica* **2016**, *3*, 283.

[70] A. Handelman, S. Lavrov, A. Kudryavtsev, A. Khatchatouriants, Y. Rosenberg, E. Mishina, G. Rosenman, *Adv. Opt. Mater.* **2013**, *1*, 875.

[71] J. Lee, M. Tymchenko, C. Argyropoulos, P.-Y. Chen, F. Lu, F. Demmerle, G. Boehm, M.-C. Amann, A. Alù, M. A. Belkin, *Nature* **2014**, *511*, 65.

[72] Z. Liu, A. W. A. Murphy, C. Kuppe, D. C. Hooper, V. K. Valev, A. Ilie, *ACS Nano* **2019**, *13*, 3896.

[73] V. K. Valev, A. Kirilyuk, F. Dalla Longa, J. T. Kohlhepp, B. Koopmans, T. Rasing, *Phys. Rev. B* **2007**, *75*, 012401.

[74] E. Ringe, B. Sharma, A.-I. Henry, L. D. Marks, R. P. Van Duyne, *Phys. Chem. Chem. Phys.* **2013**, *15*, 4110.

[75] A. O. Govorov, Z. Fan, *ChemPhysChem* **2012**, *13*, 2551.

[76] G. Baffou, R. Quidant, *Chem. Soc. Rev.* **2014**, *43*, 3898.

[77] N. I. Zheludev, Y. S. Kivshar, *Nat. Mater.* **2012**, *11*, 917.

[78] W. Gao, W. Y. Tam, *J. Opt.* **2011**, *13*, 015101.

[79] W. Fan, S. Zhang, N.-C. Panoiu, A. Abdenour, S. Krishna, R. M. Osgood, K. J. Malloy, S. R. J. Brueck, *Nano Lett.* **2006**, *6*, 1027.

[80] T. Shibanuma, G. Grinblat, P. Albella, S. A. Maier, *Nano Lett.* **2017**, *17*, 2647.

[81] L. Tong, J.-X. Cheng, *Mater. Today* **2011**, *14*, 264.

[82] E. Abbe, *Arc. Mikrosk. Anat.* **1873**, *9*, 413.

[83] L. Rayleigh, *J. R. Microsc. Soc.* **1903**, *23*, 474.

[84] P. J. Campagnola, L. M. Loew, *Nat. Biotechnol.* **2003**, *21*, 1356.

[85] J. Mertz, *Curr. Opin. Neurobiol.* **2004**, *14*, 610.

[86] E. Brown, T. McKee, E. DiTomaso, A. Pluen, B. Seed, Y. Boucher, R. K. Jain, *Nat. Med.* **2003**, *9*, 796.

[87] M. Poenie, J. Kuhn, J. Combs, *Curr. Opin. Immunol.* **2004**, *16*, 428.

[88] P. J. Campagnola, H. A. Clark, W. A. Mohler, A. Lewis, L. M. Loew, *J. Biomed. Opt.* **2001**, *6*, 277.

[89] D. Yelin, D. Oron, S. Thiberge, E. Moses, Y. Silberberg, *Opt. Express* **2003**, *11*, 1385.

[90] S.-P. Tai, Y. Wu, D.-B. Shieh, L.-J. Chen, K.-J. Lin, C.-H. Yu, S.-W. Chu, C.-H. Chang, X.-Y. Shi, Y.-C. Wen, K.-H. Lin, T.-M. Liu, C.-K. Sun, *Adv. Mater.* **2007**, *19*, 4520.

[91] S. S. Sinha, S. Jones, T. Demeritte, S. R. Chavva, Y. Shi, J. Burrell, A. Pramanik, P. C. Ray, *J. Phys. Chem. C* **2016**, *120*, 4546.

[92] E. Almeida, G. Shalem, Y. Prior, *Nat. Commun.* **2016**, *7*, 10367.

[93] S. Keren-Zur, O. Avayu, L. Michaeli, T. Ellenbogen, *ACS Photonics* **2016**, *3*, 117.

[94] L. Liu, X. Zhang, M. Kenney, X. Su, N. Xu, C. Ouyang, Y. Shi, J. Han, W. Zhang, S. Zhang, *Adv. Mater.* **2014**, *26*, 5031.

[95] X. Ni, A. V. Kildishev, V. M. Shalaev, *Nat. Commun.* **2013**, *4*, 2807.

[96] E. Almeida, O. Bitton, Y. Prior, *Nat. Commun.* **2016**, *7*, 12533.

[97] H. W. K. Tom, T. F. Heinz, Y. R. Shen, *Phys. Rev. Lett.* **1983**, *51*, 1983.

[98] O. A. Aktsipetrov, I. M. Baranova, E. D. Mishina, A. V. Petukhov, *JETP Lett.* **1984**, *40*, 1012.

[99] C. H. Lee, R. K. Chang, N. Bloembergen, *Phys. Rev. Lett.* **1967**, *18*, 167.

[100] W. Cai, A. P. Vasudev, M. L. Brongersma, *Science* **2011**, *333*, 1720.

[101] A. Kirilyuk, T. Rasing, *J. Opt. Soc. Am. B* **2005**, *22*, 148.

[102] O. A. Aktsipetrov, T. V. Murzina, E. M. Kim, R. V. Kapra, A. A. Fedyanin, M. Inoue, A. F. Kravets, S. V. Kuznetsova, M. V. Ivanchenko, V. G. Lifshits, *J. Opt. Soc. Am. B* **2005**, *22*, 138.

[103] Y. Sheng, A. Best, H.-J. Butt, W. Krolikowski, A. Arie, K. Koynov, *Opt. Express* **2010**, *18*, 16539.

[104] V. V Pavlov, J. Ferré, P. Meyer, G. Tessier, P. Georges, A. Brun, P. Beauvillain, V. Mathet, *J. Phys.: Condens. Matter* **2001**, *13*, 9867.

[105] V. K. Valev, J. J. Baumberg, C. Sibilia, T. Verbiest, *Adv. Mater.* **2013**, *25*, 2517.

[106] V. K. Valev, J. J. Baumberg, B. De Clercq, N. Braz, X. Zheng, E. J. Osley, S. Vandendriessche, M. Hojeij, C. Blejean, J. Mertens, C. G. Biris, V. Volskiy, M. Ameloot, Y. Ekinci, G. A. E. Vandenbosch, P. A. Warburton, V. V Moshchalkov, N. C. Panoiu, T. Verbiest, *Adv. Mater.* **2014**, *26*, 4074.

[107] J. T. Collins, C. Kuppe, D. C. Hooper, C. Sibilia, M. Centini, V. K. Valev, *Adv. Opt. Mater.* **2017**, *5*, 1700182.

[108] J. T. Collins, K. R. Rusimova, D. C. Hooper, H.-H. Jeong, L. Ohnoutek, F. Pradaux-Caggiano, T. Verbiest, D. R. Carbery, P. Fischer, V. K. Valev, *Phys. Rev. X* **2019**, *9*, 011024.

[109] D. L. Andrews, T. Thirunamachandran, *J. Chem. Phys.* **1979**, *70*, 1027.

[110] S. Lan, L. Kang, D. T. Schoen, S. P. Rodrigues, Y. Cui, M. L. Brongersma, W. Cai, *Nat. Mater.* **2015**, *14*, 807.

[111] Y. H. Jang, Y. J. Jang, S. Kim, L. N. Quan, K. Chung, D. H. Kim, *Chem. Rev.* **2016**, *116*, 14982.

[112] O. Demichel, M. Petit, S. Viarbitskaya, R. Méjard, F. de Fornel, E. Hertz, F. Billard, A. Bouhelier, B. Cluzel, *ACS Photonics* **2016**, *3*, 791.

[113] N. Del Fatti, F. Vallée, C. Flytzanis, Y. Hamanaka, A. Nakamura, *Chem. Phys.* **2000**, *251*, 215.

[114] D. S. Ivanov, L. V. Zhigilei, *Phys. Rev. B* **2003**, *68*, 064114.

[115] C.-K. Sun, F. Vallée, L. H. Acioli, E. P. Ippen, J. G. Fujimoto, *Phys. Rev. B* **1994**, *50*, 15337.

[116] T. Q. Qiu, C. L. Tien, *J. Heat Transfer* **1993**, *115*, 842.

[117] H. A. Atwater, A. Polman, *Nat. Mater.* **2010**, *9*, 205.

[118] S. Linic, U. Aslam, C. Boerigter, M. Morabito, *Nat. Mater.* **2015**, *14*, 567.

[119] M. Bauer, A. Marienfeld, M. Aeschlimann, *Prog. Surf. Sci.* **2015**, *90*, 319.

[120] M. L. Brongersma, N. J. Halas, P. Nordlander, *Nat. Nanotechnol.* **2015**, *10*, 25.

[121] S. Linic, P. Christopher, H. Xin, A. Marimuthu, *Acc. Chem. Res.* **2013**, *46*, 1890.

[122] A. Fujishima, K. Honda, *Nature* **1972**, *238*, 37.

[123] A. Kudo, Y. Miseki, *Chem. Soc. Rev.* **2009**, *38*, 253.

[124] A. L. Linsebigler, G. Lu, J. T. Yates, *Chem. Rev.* **1995**, *95*, 735.

[125] Y. Cho, S. Kim, B. Park, C.-L. Lee, J. K. Kim, K. Lee, I. Y. Choi, J. K. Kim, K. Zhang, S. H. Oh, J. H. Park, *Nano Lett.* **2018**, *18*, 4257.

[126] Z. Zhang, X. Jiang, B. Liu, L. Guo, N. Lu, L. Wang, J. Huang, K. Liu, B. Dong, *Adv. Mater.* **2018**, *30*, 1705221.

[127] G. Collins, J. D. Holmes, *Adv. Mater.* **2016**, *28*, 5689.

[128] M. Sun, H. Xu, *Small* **2012**, *8*, 2777.

[129] R. Long, Y. Li, L. Song, Y. Xiong, *Small* **2015**, *11*, 3873.

[130] K. Ueno, S. Juodkazis, T. Shibuya, Y. Yokota, V. Mizeikis, K. Sasaki, H. Misawa, *J. Am. Chem. Soc.* **2008**, *130*, 6928.

[131] C. Hrelescu, T. K. Sau, A. L. Rogach, F. Jäckel, G. Laurent, L. Douillard, F. Charra, *Nano Lett.* **2011**, *11*, 402.

[132] F. Shaik, I. Peer, P. K. Jain, L. Amirav, *Nano Lett.* **2018**, *18*, 4370.

[133] S. Mukherjee, L. Zhou, A. M. Goodman, N. Large, C. Ayala-Orozco, Y. Zhang, P. Nordlander, N. J. Halas, *J. Am. Chem. Soc.* **2014**, *136*, 64.

[134] S. Mubeen, J. Lee, N. Singh, S. Krämer, G. D. Stucky, M. Moskovits, *Nat. Nanotechnol.* **2013**, *8*, 247.

[135] P. Christopher, H. Xin, S. Linic, *Nat. Chem.* **2011**, *3*, 467.

[136] P. Christopher, H. Xin, A. Marimuthu, S. Linic, *Nat. Mater.* **2012**, *11*, 1044.

[137] U. Aslam, S. Chavez, S. Linic, *Nat. Nanotechnol.* **2017**, *12*, 1000.

[138] N. Ortiz, B. Zoellner, S. J. Hong, Y. Ji, T. Wang, Y. Liu, P. A. Maggard, G. Wang, *ACS Appl. Mater. Interfaces* **2017**, *9*, 25962.

[139] Q. Xiao, S. Sarina, E. R. Waclawik, J. Jia, J. Chang, J. D. Riches, H. Wu, Z. Zheng, H. Zhu, *ACS Catal.* **2016**, *6*, 1744.

[140] H. Huang, L. Zhang, Z. Lv, R. Long, C. Zhang, Y. Lin, K. Wei, C. Wang, L. Chen, Z.-Y. Li, Q. Zhang, Y. Luo, Y. Xiong, *J. Am. Chem. Soc.* **2016**, *138*, 6822.

[141] M. K. Gangishetty, A. M. Fontes, M. Malta, T. L. Kelly, R. W. J. Scott, *RSC Adv.* **2017**, *7*, 40218.

[142] F. Wang, C. Li, H. Chen, R. Jiang, L. Sun, Q. Li, J. Wang, J. C. Yu, C. Yan, *J. Am. Chem. Soc.* **2013**, *135*, 5588.

[143] X. Zhang, X. Li, M. E. Reish, D. Zhang, N. Q. Su, Y. Gutiérrez, F. Moreno, W. Yang, H. O. Everitt, J. Liu, *Nano Lett.* **2018**, *18*, 1714.

[144] D. Liu, D. Yang, Y. Gao, J. Ma, R. Long, C. Wang, Y. Xiong, *Angew. Chem., Int. Ed.* **2016**, *55*, 4577.

[145] S. K. Cushing, N. Wu, *J. Phys. Chem. Lett.* **2016**, *7*, 666.

[146] J. Li, S. K. Cushing, F. Meng, T. R. Senty, A. D. Bristow, N. Wu, *Nat. Photonics* **2015**, *9*, 601.

[147] S.-W. Baek, G. Park, J. Noh, C. Cho, C.-H. Lee, M.-K. Seo, H. Song, J.-Y. Lee, *ACS Nano* **2014**, *8*, 3302.

[148] M. W. Knight, H. Sobhani, P. Nordlander, N. J. Halas, *Science* **2011**, *332*, 702.

[149] A. Sobhani, M. W. Knight, Y. Wang, B. Zheng, N. S. King, L. V. Brown, Z. Fang, P. Nordlander, N. J. Halas, *Nat. Commun.* **2013**, *4*, 1643.

[150] K.-T. Lin, H.-L. Chen, Y.-S. Lai, C.-C. Yu, *Nat. Commun.* **2014**, *5*, 3288.

[151] W. Li, J. Valentine, *Nano Lett.* **2014**, *14*, 3510.

[152] W. Wang, A. Klots, D. Prasai, Y. Yang, K. I. Bolotin, J. Valentine, *Nano Lett.* **2015**, *15*, 7440.

[153] C. Jia, X. Li, N. Xin, Y. Gong, J. Guan, L. Meng, S. Meng, X. Guo, *Adv. Energy Mater.* **2016**, *6*, 1600431.

[154] D. Thrithamarassery Gangadharan, Z. Xu, Y. Liu, R. Izquierdo, D. Ma, *Nanophotonics* **2017**, *6*, 153.

[155] R. Groeneveld, R. Sprik, A. Lagendijk, *Phys. Rev. Lett.* **1990**, *64*, 784.

[156] G. V. Hartland, *Annu. Rev. Phys. Chem.* **2006**, *57*, 403.

[157] N. Del Fatti, C. Voisin, F. Chevy, F. Vallée, C. Flytzanis, *J. Chem. Phys.* **1999**, *110*, 11484.

[158] H. Lamb, in *Proceedings of the London Mathematical Society* Vol. *s1–13*, **1881**, p. 189.

[159] J. H. Hodak, A. Henglein, G. V. Hartland, *J. Chem. Phys.* **1999**, *111*, 8613.

[160] G. V. Hartland, *Chem. Rev.* **2011**, *111*, 3858.

[161] J. H. Hodak, A. Henglein, G. V. Hartland, *J. Phys. Chem. B* **2000**, *104*, 9954.

[162] U. Rössler, *Solid State Theory*, Springer, Berlin **2009**.

[163] G. Soavi, I. Tempra, M. F. Pantano, A. Cattoni, S. Collin, P. Biagioni, N. M. Pugno, G. Cerullo, *ACS Nano* **2016**, *10*, 2251.

[164] N. Del Fatti, C. Voisin, D. Christofilos, F. Vallée, C. Flytzanis, *J. Phys. Chem. A* **2000**, *104*, 4321.

[165] P. Zijlstra, A. L. Tchebotareva, J. W. M. Chon, M. Gu, M. Orrit, *Nano Lett.* **2008**, *8*, 3493.

[166] R. Thijssen, E. Verhagen, T. J. Kippenberg, A. Polman, *Nano Lett.* **2013**, *13*, 3293.

[167] R. Thijssen, T. J. Kippenberg, A. Polman, E. Verhagen, *Nano Lett.* **2015**, *15*, 3971.

[168] A. A. Oraevsky, A. A. Karabutov, E. V. Savateeva, *Proc. SPIE* **2001**, *4434*, 60.

[169] X. Yang, E. W. Stein, S. Ashkenazi, L. V. Wang, *Wiley Interdiscip. Rev.: Nanomed. Nanobiotechnol.* **2009**, *1*, 360.

[170] M. Eghtedari, A. Oraevsky, J. A. Copland, N. A. Kotov, A. Conjusteau, M. Motamedi, *Nano Lett.* **2007**, *7*, 1914.

[171] C. Kim, E. C. Cho, J. Chen, K. H. Song, L. Au, C. Favazza, Q. Zhang, C. M. Cobley, F. Gao, Y. Xia, L. V. Wang, *ACS Nano* **2010**, *4*, 4559.

[172] B. Wang, E. Yantsen, T. Larson, A. B. Karpiouk, S. Sethuraman, J. L. Su, K. Sokolov, S. Y. Emelianov, *Nano Lett.* **2009**, *9*, 2212.

[173] Q. Zhang, N. Iwakuma, P. Sharma, B. M. Moudgil, C. Wu, J. McNeill, H. Jiang, S. R. Grobmyer, *Nanotechnology* **2009**, *20*, 395102.

[174] Y. Zhang, G. Wang, L. Yang, F. Wang, A. Liu, *Coord. Chem. Rev.* **2018**, *370*, 1.

[175] A. Belardini, M. Centini, G. Leahu, D. C. Hooper, R. L. Voti, E. Fazio, J. W. Haus, A. Sarangan, V. K. Valev, R. Li Voti, E. Fazio, J. W. Haus, A. Sarangan, V. K. Valev, C. Sibilia, *Sci. Rep.* **2016**, *6*, 31796.

[176] A. Benedetti, B. Alam, M. Esposito, V. Tasco, G. Leahu, A. Belardini, R. Li Voti, A. Passaseo, C. Sibilia, *Sci. Rep.* **2017**, *7*, 5257.

[177] G. Leahu, E. Petronijevic, A. Belardini, M. Centini, R. Li Voti, T. Hakkarainen, E. Koivusalo, M. Guina, C. Sibilia, *Sci. Rep.* **2017**, *7*, 2833.

[178] E. Petronijević, G. Leahu, R. Li Voti, A. Belardini, C. Scian, N. Michieli, T. Cesca, G. Mattei, C. Sibilia, *Appl. Phys. Lett.* **2019**, *114*, 053101.

[179] B. Hopkins, A. N. Poddubny, A. E. Miroshnichenko, Y. S. Kivshar, *Laser Photonics Rev.* **2016**, *10*, 137.

[180] P. Lorazo, L. J. Lewis, M. Meunier, *Phys. Rev. B* **2006**, *73*, 134108.

[181] S. Hashimoto, D. Werner, T. Uwada, *J. Photochem. Photobiol., C* **2012**, *13*, 28.

[182] B. C. Stuart, M. D. Feit, S. Herman, A. M. Rubenchik, B. W. Shore, M. D. Perry, *J. Opt. Soc. Am. B* **1996**, *13*, 459.

[183] A. I. Kuznetsov, J. Koch, B. N. Chichkov, *Opt. Express* **2009**, *17*, 18820.

[184] A. Habenicht, *Science* **2005**, *309*, 2043.

[185] N. Nedyalkov, T. Sakai, T. Miyanishi, M. Obara, *J. Phys. D: Appl. Phys.* **2006**, *39*, 5037.

[186] R. K. Harrison, A. Ben-Yakar, *Opt. Express* **2010**, *18*, 22556.

[187] A. Kolloch, T. Geldhauser, K. Ueno, H. Misawa, J. Boneberg, A. Plech, P. Leiderer, *Appl. Phys. A* **2011**, *104*, 793.

[188] L. Liu, P. Peng, A. Hu, G. Zou, W. W. Duley, Y. N. Zhou, *Appl. Phys. Lett.* **2013**, *102*, 073107.

[189] P. Peng, A. Hu, A. P. Gerlich, G. Zou, L. Liu, Y. N. Zhou, *ACS Appl. Mater. Interfaces* **2015**, *7*, 12597.

[190] S. M. Huang, M. H. Hong, B. S. Luk'yanchuk, Y. W. Zheng, W. D. Song, Y. F. Lu, T. C. Chong, *J. Appl. Phys.* **2002**, *92*, 2495.

[191] P. Zijlstra, J. W. M. Chon, M. Gu, *Phys. Chem. Chem. Phys.* **2009**, *11*, 5915.

[192] V. K. Valev, A. V. Silhanek, Y. Jeyaram, D. Denkova, B. De Clercq, V. Petkov, X. Zheng, V. Volskiy, W. Gillijns, G. A. E. Vandenbosch, O. A. Aktsipetrov, M. Ameloot, V. V. Moshchalkov, T. Verbiest, *Phys. Rev. Lett.* **2011**, *106*, 226803.

[193] V. K. Valev, D. Denkova, X. Zheng, A. I. Kuznetsov, C. Reinhardt, B. N. Chichkov, G. Tsutsumanova, E. J. Osley, V. Petkov, B. De Clercq, A. V. Silhanek, Y. Jeyaram, V. Volskiy, P. A. Warburton, G. A. E. Vandenbosch, S. Russev, O. A. Aktsipetrov, M. Ameloot, V. V. Moshchalkov, T. Verbiest, *Adv. Mater.* **2012**, *24*, OP29.

[194] V. K. Valev, W. Libaers, U. Zywietz, X. Zheng, M. Centini, N. Pfullmann, L. O. Herrmann, C. Reinhardt, V. Volskiy, A. V Silhanek, B. N. Chichkov, C. Sibilia, G. a E. Vandenbosch, V. V. Moshchalkov, J. J. Baumberg, T. Verbiest, *Opt. Lett.* **2013**, *38*, 2256.

[195] K. Venkatakrishnan, B. Tan, P. Stanley, N. R. Sivakumar, *J. Appl. Phys.* **2002**, *92*, 1604.

[196] G. Kamlage, T. Bauer, A. Ostendorf, B. N. Chichkov, *Appl. Phys. B: Lasers Opt.* **2003**, *77*, 307.

[197] V. K. Valev, B. De Clercq, C. G. Biris, X. Zheng, S. Vandendriessche, M. Hojeij, D. Denkova, Y. Jeyaram, N. C. Panoiu, Y. Ekinci, A. V. Silhanek, V. Volskiy, G. A. E. Vandenbosch, M. Ameloot, V. V. Moshchalkov, T. Verbiest, *Adv. Mater.* **2012**, *24*, OP208.

[198] L. Lin, L. Liu, P. Peng, G. Zou, W. W. Duley, Y. N. Zhou, *Nanotechnology* **2016**, *27*, 125201.

[199] L. O. Herrmann, V. K. Valev, C. Tserkezis, J. S. Barnard, S. Kasera, O. A. Scherman, J. Aizpurua, J. J. Baumberg, *Nat. Commun.* **2014**, *5*, 4568.

[200] J. Fontana, R. Nita, N. Charipar, J. Naciri, K. Park, A. Dunkelberger, J. Owrutsky, A. Piqué, R. Vaia, B. Ratna, *Adv. Opt. Mater.* **2017**, *5*, 1700335.

[201] H. Goldenberg, C. J. Tranter, *Br. J. Appl. Phys.* **1952**, *3*, 296.

[202] C. M. Pitsillides, E. K. Joe, X. Wei, R. R. Anderson, C. P. Lin, *Biophys. J.* **2003**, *84*, 4023.

[203] A. O. Govorov, W. Zhang, T. Skeini, H. Richardson, J. Lee, N. A. Kotov, *Nanoscale Res. Lett.* **2006**, *1*, 84.

[204] G. Baffou, R. Quidant, C. Girard, *Appl. Phys. Lett.* **2009**, *94*, 153109.

[205] G. Baffou, R. Quidant, F. J. García de Abajo, *ACS Nano* **2010**, *4*, 709.

[206] A. O. Govorov, H. H. Richardson, *Nano Today* **2007**, *2*, 30.

[207] J. Croissant, J. I. Zink, *J. Am. Chem. Soc.* **2012**, *134*, 7628.

[208] S. Ghosh, A. Ghosh, *Sci. Rob.* **2018**, *3*, eaaq0076.

[209] T. Li, J. Li, K. I. Morozov, Z. Wu, T. Xu, I. Rozen, A. M. Leshansky, L. Li, J. Wang, *Nano Lett.* **2017**, *17*, 5092.

[210] C. Ohm, M. Brehmer, R. Zentel, *Adv. Mater.* **2010**, *22*, 3366.

[211] D. Cao, C. Xu, W. Lu, C. Qin, S. Cheng, *Sol. RRL* **2018**, *2*, 1700219.

[212] L.-W. Xia, R. Xie, X.-J. Ju, W. Wang, Q. Chen, L.-Y. Chu, *Nat. Commun.* **2013**, *4*, 2226.

**ADVANCED
SCIENCE NEWS**

www.advancedsciencenews.com

**ADVANCED
OPTICAL
MATERIALS**

www.advopticalmat.de

[213] L. Lin, X. Peng, M. Wang, L. Scarabelli, Z. Mao, L. M. Liz-Marzán, M. F. Becker, Y. Zheng, *ACS Nano* **2016**, *10*, 9659.

[214] L. Lin, M. Wang, X. Peng, E. N. Lissek, Z. Mao, L. Scarabelli, E. Adkins, S. Coskun, H. E. Unalan, B. A. Korgel, L. M. Liz-Marzán, E.-L. Florin, Y. Zheng, *Nat. Photonics* **2018**, *12*, 195.

[215] M. R. K. Ali, Y. Wu, M. A. El-Sayed, *J. Phys. Chem. C* **2019**, *123*, 15375.

[216] G. Majno, I. Joris, *Am. J. Pathol.* **1995**, *146*, 3.

[217] X. Huang, P. K. Jain, I. H. El-Sayed, M. A. El-Sayed, *Photochem. Photobiol.* **2006**, *82*, 412.

[218] M. Pérez-Hernández, P. del Pino, S. G. Mitchell, M. Moros, G. Stepien, B. Pelaz, W. J. Parak, E. M. Gálvez, J. Pardo, J. M. de la Fuente, *ACS Nano* **2015**, *9*, 52.

[219] V. P. Pattani, J. Shah, A. Atalis, A. Sharma, J. W. Tunnell, *J. Nanopart. Res.* **2015**, *17*, 20.

[220] H. Maeda, J. Wu, T. Sawa, Y. Matsumura, K. Hori, *J. Controlled Release* **2000**, *65*, 271.

[221] E. Ruoslahti, *Nat. Rev. Cancer* **2002**, *2*, 83.

[222] E. Ruoslahti, S. N. Bhatia, M. J. Sailor, *J. Cell Biol.* **2010**, *188*, 759.

[223] S. Wilhelm, A. J. Tavares, Q. Dai, S. Ohta, J. Audet, H. F. Dvorak, W. C. W. Chan, *Nat. Rev. Mater.* **2016**, *1*, 16014.

[224] X. Huang, X. Peng, Y. Wang, Y. Wang, D. M. Shin, M. A. El-Sayed, S. Nie, *ACS Nano* **2010**, *4*, 5887.

[225] C. H. J. Choi, C. A. Alabi, P. Webster, M. E. Davis, *Proc. Natl. Acad. Sci. USA* **2010**, *107*, 1235.

[226] H. Yuan, A. M. Fales, T. Vo-Dinh, *J. Am. Chem. Soc.* **2012**, *134*, 11358.

[227] Y. Wang, K. C. L. Black, H. Luehmann, W. Li, Y. Zhang, X. Cai, D. Wan, S.-Y. Liu, M. Li, P. Kim, Z.-Y. Li, L. V. Wang, Y. Liu, Y. Xia, *ACS Nano* **2013**, *7*, 2068.

[228] A. M. Smith, M. C. Mancini, S. Nie, *Nat. Nanotechnol.* **2009**, *4*, 710.

[229] L. R. Hirsch, R. J. Stafford, J. A. Bankson, S. R. Sershen, B. Rivera, R. E. Price, J. D. Hazle, N. J. Halas, J. L. West, *Proc. Natl. Acad. Sci. USA* **2003**, *100*, 13549.

[230] X. Huang, I. H. El-Sayed, W. Qian, M. A. El-Sayed, *J. Am. Chem. Soc.* **2006**, *128*, 2115.

[231] H. Jo, H. Youn, S. Lee, C. Ban, *J. Mater. Chem. B* **2014**, *2*, 4862.

[232] J. Chen, C. Glaus, R. Laforest, Q. Zhang, M. Yang, M. Gidding, M. J. Welch, Y. Xia, *Small* **2010**, *6*, 811.

[233] C. Ayala-Orozco, C. Urban, M. W. Knight, A. S. Urban, O. Neumann, S. W. Bishnoi, S. Mukherjee, A. M. Goodman, H. Charron, T. Mitchell, M. Shea, R. Roy, S. Nanda, R. Schiff, N. J. Halas, A. Joshi, *ACS Nano* **2014**, *8*, 6372.

[234] P. Vijayaraghavan, C.-H. Liu, R. Vankayala, C.-S. Chiang, K. C. Hwang, *Adv. Mater.* **2014**, *26*, 6689.

[235] N. Gandra, C. Portz, S. Z. Nergiz, A. Fales, T. Vo-Dinh, S. Singamaneni, *Sci. Rep.* **2015**, *5*, 10311.

[236] E. Ye, K. Y. Win, H. R. Tan, M. Lin, C. P. Teng, A. Mlayah, M.-Y. Han, *J. Am. Chem. Soc.* **2011**, *133*, 8506.

[237] J. M. Stern, J. Stanfield, W. Kabbani, J.-T. Hsieh, J. A. Cadeddu, *J. Urol.* **2008**, *179*, 748.

[238] A. S. Abdoon, E. A. Al-Ashkar, O. M. Kandil, A. M. Shaban, H. M. Khaled, M. A. El Sayed, M. M. El Shaer, A. H. Shaalan, W. H. Eisa, A. A. G. Eldin, H. A. Hussein, M. R. El Ashkar, M. R. Ali, A. A. Shabaka, *Nanomedicine* **2016**, *12*, 2291.

[239] Z. Zhang, J. Wang, C. Chen, *Adv. Mater.* **2013**, *25*, 3869.

[240] D. Luo, K. A. Carter, D. Miranda, J. F. Lovell, *Adv. Sci.* **2017**, *4*, 1600106.

[241] S. Shen, H. Tang, X. Zhang, J. Ren, Z. Pang, D. Wang, H. Gao, Y. Qian, X. Jiang, W. Yang, *Biomaterials* **2013**, *34*, 3150.

[242] H. Sun, J. Su, Q. Meng, Q. Yin, L. Chen, W. Gu, Z. Zhang, H. Yu, P. Zhang, S. Wang, Y. Li, *Adv. Funct. Mater.* **2017**, *27*, 1604300.

[243] A. K. Rengan, A. B. Bukhari, A. Pradhan, R. Malhotra, R. Banerjee, R. Srivastava, A. De, *Nano Lett.* **2015**, *15*, 842.

[244] H. H. Richardson, Z. N. Hickman, A. O. Govorov, A. C. Thomas, W. Zhang, M. E. Kordesch, *Nano Lett.* **2006**, *6*, 783.

[245] G. Ni, N. Miljkovic, H. Ghasemi, X. Huang, S. V. Boriskina, C.-T. Lin, J. Wang, Y. Xu, M. M. Rahman, T. Zhang, G. Chen, *Nano Energy* **2015**, *17*, 290.

[246] N. J. Hogan, A. S. Urban, C. Ayala-Orozco, A. Pimpinelli, P. Nordlander, N. J. Halas, *Nano Lett.* **2014**, *14*, 4640.

[247] O. Neumann, C. Feronti, A. D. Neumann, A. Dong, K. Schell, B. Lu, E. Kim, M. Quinn, S. Thompson, N. Grady, P. Nordlander, M. Oden, N. J. Halas, *Proc. Natl. Acad. Sci. USA* **2013**, *110*, 11677.

[248] O. Neumann, A. D. Neumann, S. Tian, C. Thibodeaux, S. Shubhankar, J. Müller, E. Silva, A. Alabastri, S. W. Bishnoi, P. Nordlander, N. J. Halas, *ACS Energy Lett.* **2017**, *2*, 8.

[249] M. S. Zielinski, J.-W. Choi, T. La Grange, M. Modestino, S. M. H. Hashemi, Y. Pu, S. Birkhold, J. A. Hubbell, D. Psaltis, *Nano Lett.* **2016**, *16*, 2159.

[250] M. Chen, Y. Wu, W. Song, Y. Mo, X. Lin, Q. He, B. Guo, *Nanoscale* **2018**, *10*, 6186.

[251] L. Zhang, J. Xing, X. Wen, J. Chai, S. Wang, Q. Xiong, *Nanoscale* **2017**, *9*, 12843.

[252] K. Bae, G. Kang, S. K. Cho, W. Park, K. Kim, W. J. Padilla, *Nat. Commun.* **2015**, *6*, 10103.

[253] L. Zhou, Y. Tan, D. Ji, B. Zhu, P. Zhang, J. Xu, Q. Gan, Z. Yu, J. Zhu, *Sci. Adv.* **2016**, *2*, e1501227.

[254] L. Zhou, Y. Tan, J. Wang, W. Xu, Y. Yuan, W. Cai, S. Zhu, J. Zhu, *Nat. Photonics* **2016**, *10*, 393.

[255] M. Zhu, Y. Li, F. Chen, X. Zhu, J. Dai, Y. Li, Z. Yang, X. Yan, J. Song, Y. Wang, E. Hitz, W. Luo, M. Lu, B. Yang, L. Hu, *Adv. Energy Mater.* **2018**, *8*, 1701028.

[256] L. Pan, D. B. Bogy, *Nat. Photonics* **2009**, *3*, 189.

[257] N. Zhou, X. Xu, A. T. Hammack, B. C. Stipe, K. Gao, W. Scholz, E. C. Gage, *Nanophotonics* **2014**, *3*, 141.

[258] W. A. Challener, C. Peng, A. V. Itagi, D. Karns, W. Peng, Y. Peng, X. Yang, X. Zhu, N. J. Gokemeijer, Y.-T. Hsia, G. Ju, R. E. Rottmayer, M. A. Seigler, E. C. Gage, *Nat. Photonics* **2009**, *3*, 220.

[259] B. C. Stipe, T. C. Strand, C. C. Poon, H. Balamane, T. D. Boone, J. A. Katine, J.-L. Li, V. Rawat, H. Nemoto, A. Hirotsune, O. Hellwig, R. Ruiz, E. Dobisz, D. S. Kercher, N. Robertson, T. R. Albrecht, B. D. Terris, *Nat. Photonics* **2010**, *4*, 484.

[260] K. R. Rusimova, D. Slavov, F. Pradaux-Caggiano, J. T. Collins, S. N. Gordeev, D. R. Carbery, W. J. Wadsworth, P. J. Mosley, V. K. Valev, *Nat. Commun.* **2019**, *10*, 2328.

1901166 (27 of 27)